

# The Impact of the Madden–Julian Oscillation on High-Latitude Winter Blocking during El Niño–Southern Oscillation Events

STEPHANIE A. HENDERSON

*Center for Climatic Research, University of Wisconsin–Madison, Madison, Wisconsin*

ERIC D. MALONEY

*Department of Atmospheric Science, Colorado State University, Fort Collins, Colorado*

(Manuscript received 23 October 2017, in final form 9 February 2018)

## ABSTRACT

Wintertime high-latitude blocking is associated with persistent changes in temperature and precipitation over much of the Northern Hemisphere. Studies have shown that the Madden–Julian oscillation (MJO), the primary form of intraseasonal tropical variability, significantly modulates the frequency of high-latitude blocking through large-scale Rossby waves that alter the global circulation. However, the characteristics of MJO teleconnections are altered by El Niño–Southern Oscillation (ENSO), which modifies the global flow on interannual time scales, suggesting that the MJO influence on blocking may depend on the ENSO phase. The characteristics of MJO Rossby waves and blocking during ENSO events are examined using composite analysis and a nonlinear baroclinic model. The ENSO phase-dependent teleconnection patterns are found to significantly impact Pacific and Atlantic high-latitude blocking. During El Niño, a significant persistent increase in Pacific and Atlantic blocking follows the real-time multivariate MJO (RMM) phase 7, characterized by anomalous enhanced tropical convection over the East Indian Ocean and suppressed west Pacific convection. The maximum Atlantic blocking increase is triple the climatological winter mean. Results suggest that the MJO provides the initial dipole anomaly associated with the Atlantic blocking increase, and transient eddy activity aids in its persistence. However, during La Niña significant blocking anomalies are primarily observed during the first half of an MJO event. Significant suppression of Pacific and Atlantic blocking follows RMM phase 3, when east Indian Ocean MJO convection is suppressed and west Pacific convection is enhanced. The physical basis for these results is explained.

## 1. Introduction

Intraseasonal variability in the tropical atmosphere is primarily governed by the Madden–Julian oscillation (MJO; Madden and Julian 1971, 1972). The MJO has a period of approximately 30–60 days and is typically characterized by enhanced tropical convection flanked by suppressed convection that propagates eastward from the west Indian Ocean to the central Pacific, with a tropical circumglobal signal in the upper-level winds. The convective heating anomalies can generate large-scale Rossby waves, or teleconnections, that significantly influence the extratropical circulation (e.g., Hoskins and Karoly 1981; Matthews et al. 2004; Seo and Son 2012). Recently, MJO teleconnections have been linked to significant changes in

Northern Hemisphere winter blocking (Henderson et al. 2016, hereinafter H16; Hamill and Kiladis 2014) and Rossby wave breaking (e.g., Moore et al. 2010; Cassou 2008), which is associated with blocking events. Atmospheric blocks can lead to extreme weather events due to their persistent and quasi-stationary nature (e.g., Hoskins and Sardeshmukh 1987; Buehler et al. 2011).

During a blocking event, the mean westerly flow is “blocked” for up to several weeks, redirecting air masses and precipitation (e.g., Berggren et al. 1949; Masato et al. 2012). Classic midlatitude blocking blocks the eddy-driven jet, whereas high-latitude blocking diverts its flow (e.g., Woollings et al. 2008; Woollings and Hoskins 2008; Davini et al. 2012). H16 demonstrated that high-latitude winter blocking over the Pacific is significantly suppressed when MJO teleconnections strengthen the 500-hPa geopotential height gradient, given that a height reversal at this level is often used to

---

*Corresponding author:* Stephanie A. Henderson, sahenderson@wisc.edu

DOI: 10.1175/JCLI-D-17-0721.1

© 2018 American Meteorological Society. For information regarding reuse of this content and general copyright information, consult the [AMS Copyright Policy](#) ([www.ametsoc.org/PUBSReuseLicenses](http://www.ametsoc.org/PUBSReuseLicenses)).

define blocking (e.g., Masato et al. 2013; Tibaldi and Molteni 1990). This typically occurs when MJO convection is enhanced over the Indian Ocean and Maritime Continent. When MJO convection is suppressed in this region and enhanced in the Pacific Ocean, MJO teleconnections weaken the height gradient and high-latitude Pacific blocking is more likely to occur. In addition, the frequency of blocking in the Atlantic is nearly doubled relative to the winter mean when MJO convection is suppressed over the Maritime Continent and enhanced in the west Pacific. When MJO convective anomalies are of the opposite sign, blocking is significantly suppressed (e.g., H16; Hamill and Kiladis 2014). Atmospheric blocking is often associated with Rossby wave breaking (e.g., Berrisford et al. 2007). Moore et al. (2010) demonstrated that during the MJO cycle there are significant changes in Rossby wave breaking poleward of the jet where high-latitude blocking occurs (e.g., Woollings et al. 2008; Woollings and Hoskins 2008), with less frequent central and eastern North Pacific cyclonic wave breaking during the early MJO cycle and increased western and central North Pacific cyclonic wave breaking later in the MJO cycle. The study suggested that these changes in wave breaking are accompanied by changes in atmospheric blocking frequency and surface cyclone density.

The results discussed above suggest that MJO teleconnections may be an important tool in the midrange forecasting of high-latitude blocking. However, the characteristics of MJO teleconnection patterns and the associated changes in blocking may be different when the mean large-scale circulation is altered, such as during El Niño–Southern Oscillation (ENSO) events.

ENSO is an ocean–atmosphere coupled mode in the tropical Pacific and the principal pattern of global interannual variability (e.g., Rasmusson and Wallace 1983). Like the MJO, convective anomalies associated with ENSO act as heat sources that emit Rossby waves altering the extratropical circulation. The global changes associated with ENSO persist for time scales longer than the MJO, thereby affecting the basic state that the MJO feels and altering the pathways of MJO Rossby wave propagation. Takahashi and Shirooka (2014) and Moon et al. (2011) noted differences in the pathways of MJO teleconnections due to ENSO, and Roundy et al. (2010) demonstrated the nonlinearity of the combined patterns. In addition, Riddle et al. (2013) found that ENSO modulates many MJO extratropical impacts, such as the frequency of the Pacific–North American (PNA) pattern following MJO activity. ENSO events are also associated with changes in MJO convection; during El Niño, MJO activity extends farther eastward (e.g., Hendon et al. 1999; Kessler 2001) and propagates faster (e.g., Pohl and Matthews 2007).

This study expands on the results of H16 by examining the altered pathways of MJO Rossby waves during ENSO events and their impact on Northern Hemisphere winter blocking frequency. Section 2 describes the data and indices utilized as well as the two-dimensional (2D) blocking index employed. ENSO-induced changes to the background flow and Rossby wave propagation are discussed in section 3. Section 4 examines the teleconnection patterns associated with the MJO during ENSO phases, and section 5 investigates how the MJO teleconnections alter blocking in the North Pacific and North Atlantic regions. Certain aspects of the MJO teleconnection patterns are further examined using a nonlinear baroclinic model (NLBM) in section 6. Last, concluding remarks are provided in section 7 and the main findings are summarized.

## 2. Methodology

### a. Data

The primary dataset used here is the ERA-Interim reanalysis (Dee et al. 2011) during boreal winter [December–February (DJF)], provided at  $1.5^\circ \times 1.5^\circ$  horizontal grid spacing. The data used span the period December 1979 to February 2016. Satellite-based outgoing longwave radiation (OLR) data are obtained from the National Oceanic and Atmospheric Administration (NOAA) National Climatic Data Center (NCDC; Lee 2011) on a  $1^\circ \times 1^\circ$  horizontal grid and span from 1979 to 2014.

The real-time multivariate MJO (RMM) indices are used to define the eight phases of the MJO (Wheeler and Hendon 2004; <http://www.bom.gov.au/climate/mjo/>), as in H16. The RMM indices (RMM1 and RMM2) are the first two principal components (PCs) of the combined empirical orthogonal functions (EOFs) of near-equatorial ( $15^\circ\text{S}$ – $15^\circ\text{N}$ ) anomalous OLR and 200- and 850-hPa zonal winds. The phases of the MJO, referred to here as RMM phases, are prescribed by  $\tan^{-1}(\text{RMM2}/\text{RMM1})$  and give a broad indication of the location of anomalous MJO convection. Only strong MJO events are examined here, defined when the RMM amplitude  $\sqrt{(\text{RMM1}^2 + \text{RMM2}^2)}$  is greater than 1. Note that the RMM indices are largely circulation driven (Straub 2013), suggesting that OLR-based MJO indices may provide some differences in results from those presented here. Moreover, the eastward extension of the MJO during ENSO events is represented in the third PC (e.g., Kessler 2001), suggesting that RMM1 and RMM2 may not capture the full MJO signal during ENSO events.

ENSO seasons are defined using the NOAA Climate Prediction Center (CPC) Oceanic Niño Index (ONI; [http://www.cpc.noaa.gov/products/analysis\\_monitoring/ensostuff/ensoyears.shtml](http://www.cpc.noaa.gov/products/analysis_monitoring/ensostuff/ensoyears.shtml)), which consists of a single

value for each season. The index represents the 3-month running mean of sea surface temperature (SST) in the Niño-3.4 region (5°N–5°S, 90°–150°W). A winter season experiencing warm ENSO phase conditions occurs when the ONI exceeds 0.7°C, cold ENSO conditions when the ONI is less than −0.7°C, and neutral or normal conditions when it does not meet either threshold. We note that this is a simplification of ENSO, which actually consists of a continuum of varying amplitudes and structures, including east and central Pacific patterns (e.g., Capotondi et al. 2015). The results presented here are generalized in that the characteristics of the MJO and its teleconnection patterns will vary depending on ENSO structure and amplitude. Of the 37 DJF seasons examined here, 10 are characterized by warm ENSO conditions, 9 by cold ENSO conditions, and 18 by neutral conditions.

### b. Two-dimensional blocking index

Following H16, the 2D blocking index defined by Masato et al. (2013) is utilized to examine the impact of the MJO on Northern Hemisphere blocking during ENSO phases. The blocking index is defined by

$$B_i = \frac{2}{\Delta\phi} \int_{\phi_0}^{\phi_0 + \Delta\phi/2} Z_i \partial\phi - \frac{2}{\Delta\phi} \int_{\phi_0 - \Delta\phi/2}^{\phi_0} Z_i \partial\phi, \quad (1)$$

where  $Z$  is 500-hPa geopotential height and  $\phi$  is latitude. For a given longitude, an instantaneous block occurs when the integrated geopotential height north of  $\phi_0$  is larger than the integrated height to its south, so that  $B_i > 0$ . Consistent with H16 and Masato et al. (2013),  $\phi_0$  is varied between 40° and 70°N and  $\Delta\phi = 30^\circ$ . The tracking algorithm used here is described in detail in H16. Only large-scale blocking events are examined, defined when at least 15° of longitude are blocked consecutively for at least 5 days. To calculate a blocking frequency, a dichotomous index is generated for each region where a 1 is given if all of the blocking criteria are met, and a 0 if they are not. Note that this index captures blocking events based on a reversal of the geopotential height gradient, and therefore will miss some omega-type blocking events that do not demonstrate a reversal (e.g., Small et al. 2014). Limitations of various blocking indices, including reversal type indices, are discussed in Barriopedro et al. (2010).

## 3. Rossby wave propagation during ENSO

### a. ENSO changes to the basic state

The teleconnection patterns associated with the warm and cold phases of ENSO impact the basic state, or

background flow, that the MJO experiences, thereby altering the propagation characteristics of the MJO-induced Rossby waves. The teleconnection patterns associated with the DJF warm and cold ENSO phases are shown in Fig. 1. The 500-hPa geopotential height anomalies are shown since that is the field used to define blocking in (1), useful for the discussion in section 5. During El Niño (top), an anomalous cyclonic anomaly persists over the central Pacific basin, weakening the mean meridional geopotential height gradient between the Pacific high latitudes and the midlatitudes. Furthermore, the Pacific subtropical jet extends farther eastward relative to neutral ENSO conditions (Fig. 2, shading, middle). Over North America, an anomalous anticyclone exists with an anomalous cyclone to its southeast, resembling the positive phase of the PNA pattern. During La Niña, the opposite-signed teleconnection pattern exists with a negative PNA-like pattern (Fig. 1, bottom) and is associated with a zonally contracted and stronger subtropical jet relative to El Niño conditions (Fig. 2, bottom panel). The anticyclonic anomaly also strengthens the mean meridional geopotential height gradient between the middle and high latitudes.

### b. Rossby wave propagation during ENSO events

The characteristics of Rossby wave propagation are largely determined by the upper-level zonal winds (e.g., Hoskins and Ambrizzi 1993). The impact of the zonal wind on the propagation of Rossby waves is examined using the stationary wavenumber  $K_s$  on Mercator coordinates, which provides a basic qualitative understanding of the behavior of Rossby waves. The value of  $K_s$  is calculated following Karoly (1983) and Hoskins and Ambrizzi (1993):

$$K_s = \left( \frac{a\beta_M}{\bar{u}_M} \right)^{1/2}, \quad (2)$$

where  $\bar{u}_M$  is the mean DJF 200-hPa Mercator zonal wind during El Niño or La Niña,  $a$  is Earth's radius, and  $\beta_M$  is the meridional gradient of absolute vorticity on a sphere, defined as

$$\beta_M = \frac{2\Omega \cos^2 \theta}{a} - \frac{\partial}{\partial y} \left[ \frac{1}{\cos^2 \theta} \frac{\partial}{\partial y} (\cos^2 \theta \bar{u}_M) \right], \quad (3)$$

where  $\Omega$  is Earth's rotational constant and  $\theta$  is latitude. Figure 3 shows  $K_s$  for El Niño (top) and La Niña (bottom). Regions with mean easterly winds ( $\bar{u}_M < 0$ ) are in white, and regions where the meridional gradient of absolute vorticity is reversed ( $\beta_M < 0$ ) are in black. In the subtropical jet, a vorticity anomaly forced by large-scale

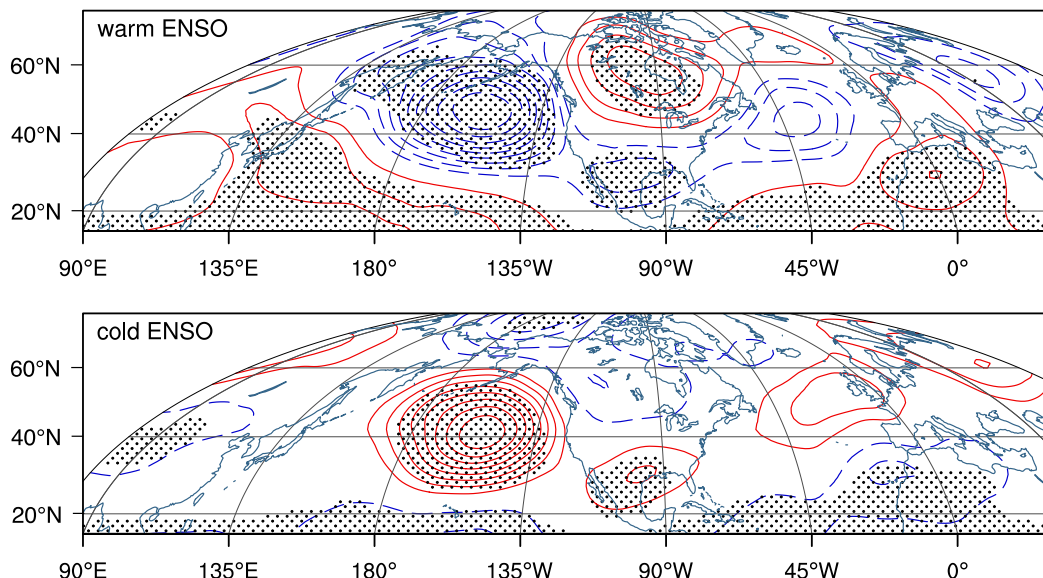


FIG. 1. DJF 500-hPa geopotential height anomalies for (top) warm and (bottom) cold ENSO. Positive values are solid red contours; negative contours are blue and dashed. Contours are every 10 m, and the zero contour is omitted. Anomalies are computed by removing the first three harmonics of the seasonal cycle and the long-term mean. Dotted regions indicate anomalies found to be 95% significantly different from zero based on a block-bootstrap test using a block length of 30 days. For a description of the block-bootstrap test, see section 5 text.

tropical convection can generate a wave train that propagates eastward within the jet, where  $K_s$  is maximized and acts as a waveguide. Based on linear wave dynamics, Rossby waves cannot propagate in regions where  $\beta_M < 0$ , which is often observed on the northern flank of the jet. The  $\beta_M < 0$  region during El Niño (Fig. 3, top) extends approximately  $40^\circ$  farther eastward than during La Niña (Fig. 3, bottom). This suggests that on average, there cannot be northward linear propagation of Rossby waves during El Niño until they travel farther east relative to La Niña. As a result, it is expected that intraseasonal teleconnection patterns in the Pacific will be shifted eastward during El Niño events relative to La Niña events. This is in agreement with Henderson et al. (2017), who found that general circulation models (GCMs) exhibiting a subtropical jet that extends too far east produce an eastward shift in the Pacific teleconnection patterns forced by MJO heating.

### c. MJO heating and RWS

In addition to basic state changes, previous studies have demonstrated that ENSO modifies the characteristics of MJO heating (e.g., Hendon et al. 1999). The longitudinal extent of 30–70-day filtered tropically averaged OLR can be visualized in Fig. 4 for warm (top panel) and cold (bottom panel) ENSO phases, where the y axis is the eight phases of the MJO. The bandpass filter is applied in order to isolate the OLR anomalies associated with intraseasonal variability. In agreement with previous studies, Fig. 4 suggests that MJO convection extends farther

eastward during warm ENSO events than cold ENSO events (e.g., Hendon et al. 1999; Kessler 2001). For brevity, we will primarily focus on RMM phases 3 and 7, which are often used to represent the first and second halves of an MJO event and are associated with the strongest extratropical MJO response into the Atlantic (e.g., Lin et al. 2009, 2010; H16). Furthermore, Tseng et al. (2018) demonstrate that these phases are associated with a consistent North Pacific response from one MJO event to the next. These phases are also chosen to allow a comparison to the results of H16.

Anomalous 30–70-day band-passed filtered OLR values associated with RMM phase 7 during both phases of ENSO are shown in Fig. 5a as an example of the ENSO influence on MJO heating. The warm and cold ENSO composites are composed of 83 and 88 days, respectively. During MJO events, upper-level divergence associated with anomalous convection leads to vorticity anomalies within the subtropical jet that initiate Rossby wave trains. The initial vorticity forcing in the jet region is examined using the Rossby wave source (RWS; Sardeshmukh and Hoskins 1988), which is the sum of the advection of absolute vorticity and vortex stretching by the divergent wind:

$$\text{RWS} = -\nabla \cdot (\mathbf{V}_x \zeta) = -\mathbf{V}_x \cdot \nabla \zeta - \zeta D, \quad (4)$$

where  $\zeta$  is the absolute vorticity,  $\mathbf{V}_x$  is the divergent component of the horizontal wind, and the divergence is

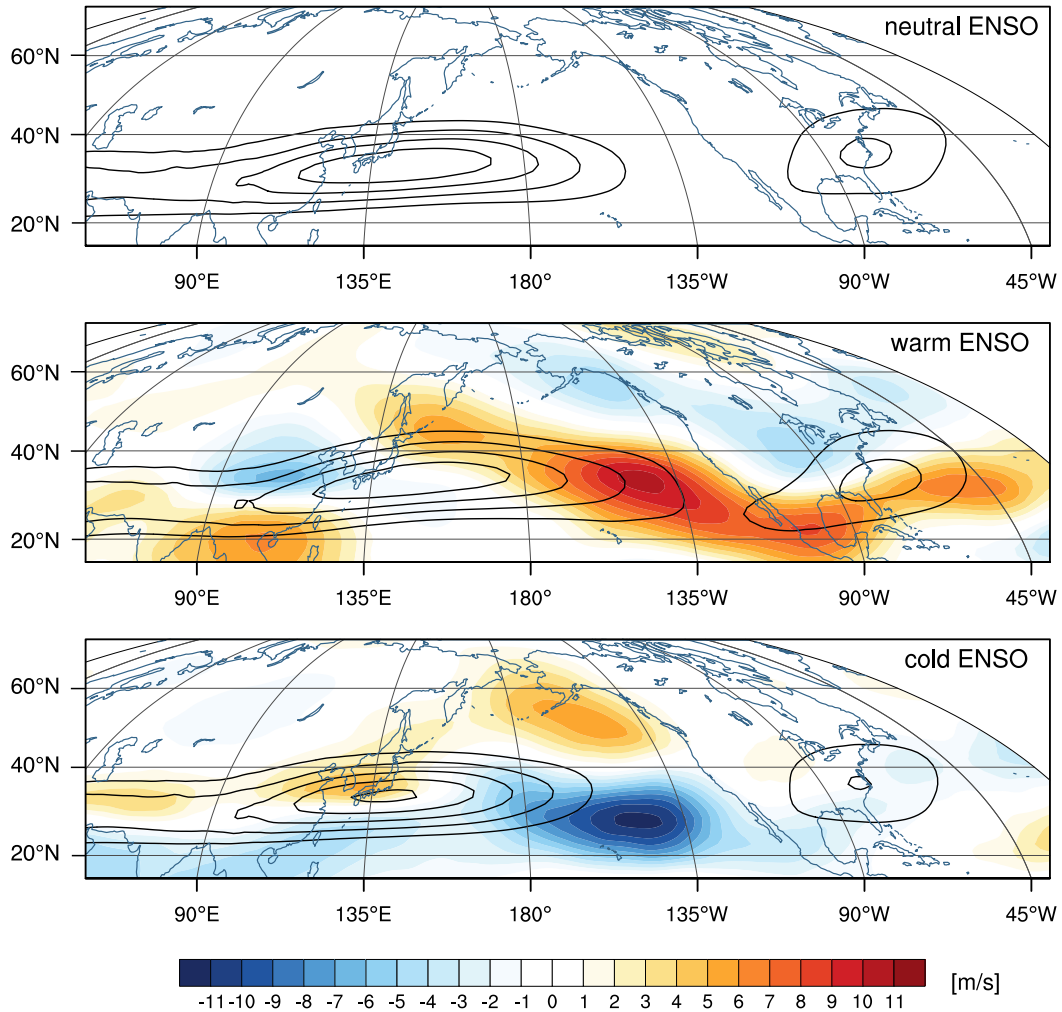


FIG. 2. Mean DJF 200-hPa zonal wind (contours) for (top) neutral, (middle) warm, and (bottom) cold ENSO conditions. Contours are every  $10 \text{ m s}^{-1}$  beginning at  $35 \text{ m s}^{-1}$ . Color shading is the mean zonal wind difference between the corresponding ENSO phase and the neutral ENSO phase.

defined by  $D = \nabla \cdot \mathbf{V}_\chi$ . The amplitude of the RWS is strongly modulated by the strength and sharpness of the subtropical jet (Sardeshmukh and Hoskins 1988). The 200-hPa 30–70-day filtered RWS associated with RMM phase 7 during both ENSO phases is provided in Fig. 5b. Also shown for reference is the  $K_s = 3$  contour as an estimate of the average turning latitude of MJO Rossby waves, which are typically characterized as wavenumber 2–4 (e.g., Seo et al. 2016; Henderson et al. 2017), and the  $\beta_M < 0$  region (hatched; see Fig. 3).

During El Niño, the RMM phase 7 RWS is centered east of the RWS during La Niña. The positive RWS near the date line is apparently due to the stronger negative OLR anomaly during El Niño, which leads to stretching of the column [Eq. (4), second term; not shown] just south of the maximum jet winds. The farther eastward extent of the RWS during El Niño

occurs during most RMM phases primarily due to the eastward extension of OLR anomalies (e.g., Fig. 4). There are also differences between ENSO phases in the RWS near and to the east of the exit region of the jet, which may be associated with differences in convection east of the date line (Fig. 4; e.g., Henderson et al. 2017). In general, the RWS associated with most RMM phases (only phase 7 shown; Fig. 5b) is stronger during La Niña than El Niño, which may be in part due to a stronger and sharper jet (Fig. 2) or stronger convection (e.g., Fig. 4). However, the number of days available for some RMM phases varies between warm and cold ENSO, which can impact the relative amplitude of a composite (e.g., Roundy et al. 2010). While there are a similar number of days during RMM phase 7 for El Niño and La Niña, El Niño events experience approximately twice the number of RMM

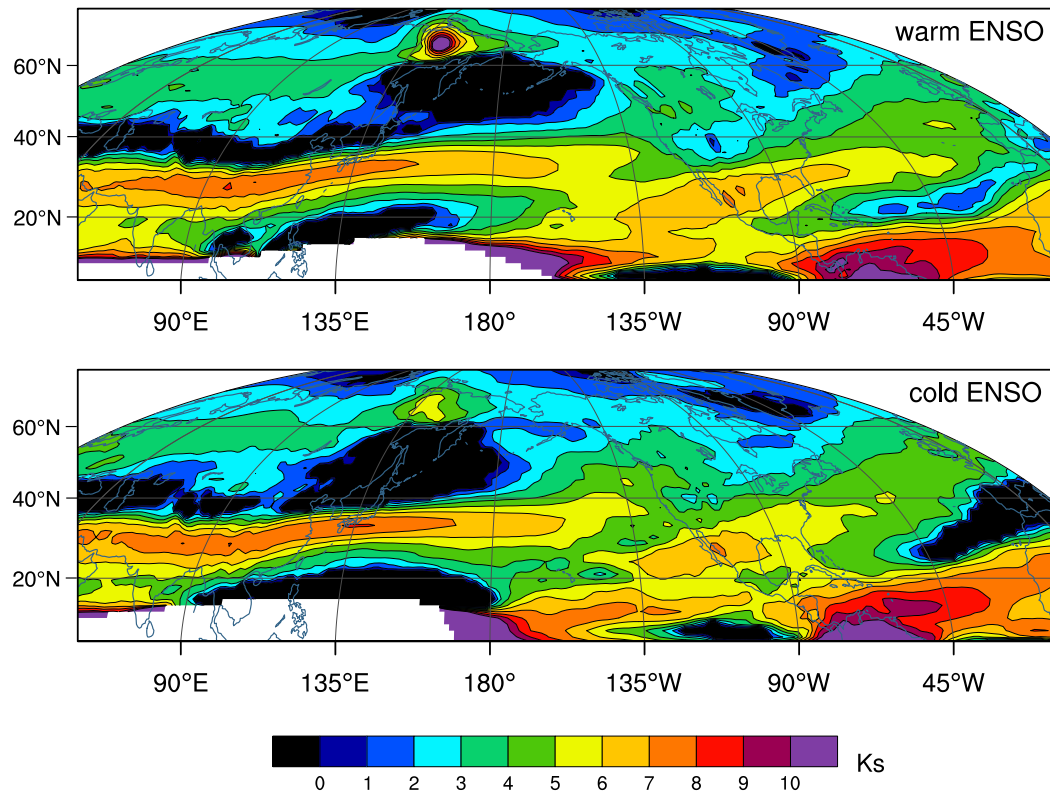


FIG. 3. Stationary zonal wavenumber  $K_s$  derived from the DJF 200-hPa Mercator zonal wind for (top) warm and (bottom) cold ENSO conditions. Regions of easterly winds ( $\bar{u}_M < 0$ ) are in white, and areas where  $\beta_M < 0$  are in black.

phase 3 days relative to La Niña. For further discussion of sample sizes, see section 6 and the appendix.

#### 4. MJO teleconnections during ENSO

The RWS anomalies associated with MJO heating (Fig. 5b) indicate the location of initial vorticity forcing for the MJO teleconnection patterns. MJO teleconnection patterns during ENSO events are examined using 30–70-day filtered 200-hPa streamfunction and 500-hPa geopotential height anomaly pentads lagged relative to RMM phases 3 and 7. This is the same compositing technique used in H16, but with the inclusion of a bandpass filter to remove the circulation anomalies associated with ENSO. As in H16, the direction of Rossby wave propagation is investigated using wave activity flux vectors ( $\mathbf{W}$  vectors; Takaya and Nakamura 2001):

$$\mathbf{W} = \frac{1}{2|\mathbf{U}|} \begin{bmatrix} U(\psi_x^2 - \psi\psi_{xx}) + V(\psi_x\psi_y - \psi\psi_{xy}) \\ U(\psi_x\psi_y - \psi\psi_{xy}) + V(\psi_y^2 - \psi\psi_{yy}) \end{bmatrix}, \quad (5)$$

where  $\psi$  is the 200-hPa anomalous pentad streamfunction, the vector  $\mathbf{U}$  is composed of the average DJF

200-hPa zonal and meridional winds represented by  $U$  and  $V$ , respectively, and the subscripts represent partial derivatives of  $\psi$  in the  $x$  and/or  $y$  directions. The  $\mathbf{W}$  vectors are parallel to the Rossby wave group velocity, providing a snapshot in time of Rossby wave packet propagation. The RMM phase 3 and 7 teleconnection pattern composites are shown in Figs. 6–9 for warm and cold ENSO events. Pentad 200-hPa streamfunction anomalies and the associated  $\mathbf{W}$  vectors are shown in the left column of each figure. Anomalous 500-hPa geopotential height is also provided (right column) since it is the field used to define blocking in (1). As in H16, dotted regions indicate geopotential height anomalies that are significantly different from zero at the 95% confidence level using a two-tailed Student's  $t$  test. The number of samples is estimated by dividing the number of days in each RMM phase by the average duration of an RMM phase across all RMM phases, which is found to be 5 (e.g., H16; Alaka and Maloney 2012). This average value is found to be the same during both El Niño and La Niña events, although the duration of an individual RMM phase varies depending on RMM and ENSO phase.

During RMM phase 3, an anticyclonic anomaly develops at the exit region of the jet during both

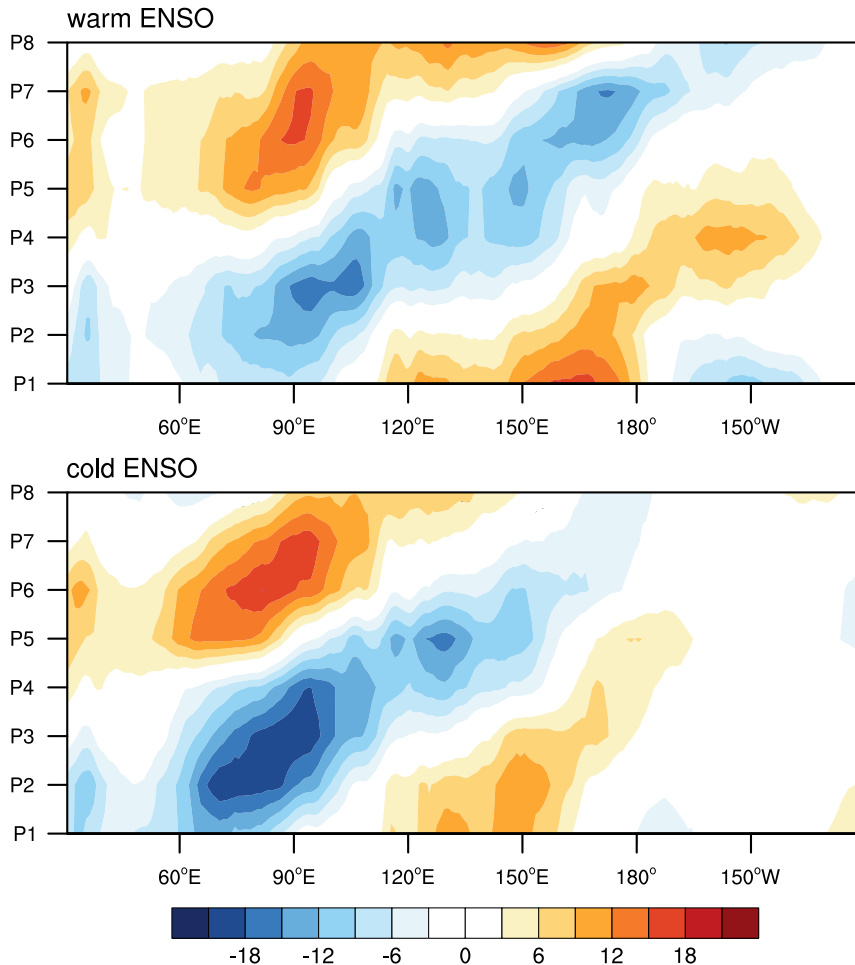


FIG. 4. RMM phase-longitude diagram of 30–70-day band filtered OLR ( $\text{W m}^{-2}$ ) averaged from  $10^{\circ}\text{S}$  to  $10^{\circ}\text{N}$  during (top) warm and (bottom) cold ENSO phases. RMM phase is along the y axis, where P1 indicates RMM phase 1 and so on.

ENSO phases (Figs. 6 and 7, top panels). The anticyclonic anomaly extends farther east during El Niño (Fig. 6) than La Niña (Fig. 7), likely due to the large difference in the zonal extent of the subtropical jet (Fig. 2; e.g., Henderson et al. 2017), in agreement with the discussion of Fig. 3. This behavior becomes even more apparent during pentad 1. Rossby waves propagate northeast from the anticyclonic anomaly forming a wave train over North America, as shown by the  $\mathbf{W}$  vectors (Figs. 6 and 7, top panel). These Pacific Rossby wave patterns are in agreement with those in Takahashi and Shirooka (2014, their Fig. 11). During El Niño, Rossby waves in pentad 1 (Fig. 6, second panel) propagate northeast from the anomalous anticyclone over northeast North America, forming a deep trough in the Atlantic. During La Niña (Fig. 7), the anticyclonic anomaly over northeast North America strengthens by pentad 1 (second

panel) and weakens over time, with no other significant anomalies in the Atlantic region.

The RMM phase 7 teleconnection patterns during El Niño and La Niña are shown in Figs. 8 and 9, respectively. For both ENSO phases,  $\mathbf{W}$  vectors suggest northeast Rossby wave packet propagation from the cyclonic anomaly near the jet exit region to the anticyclonic anomaly over northwest North America (Figs. 8 and 9; pentads 0 and 1). However, the cyclonic anomaly during La Niña extends farther west relative to that of El Niño in the midlatitudes, a difference likely due to the lesser eastward extent of the jet during La Niña (Figs. 2 and 3). In addition, the teleconnection pattern during La Niña is of higher amplitude than that during El Niño. This difference in amplitude may be due to the stronger RWS during La Niña (Fig. 5), given that RMM phase 7 has a similar number of days during both ENSO phases. During El Niño, MJO Rossby wave packets propagate

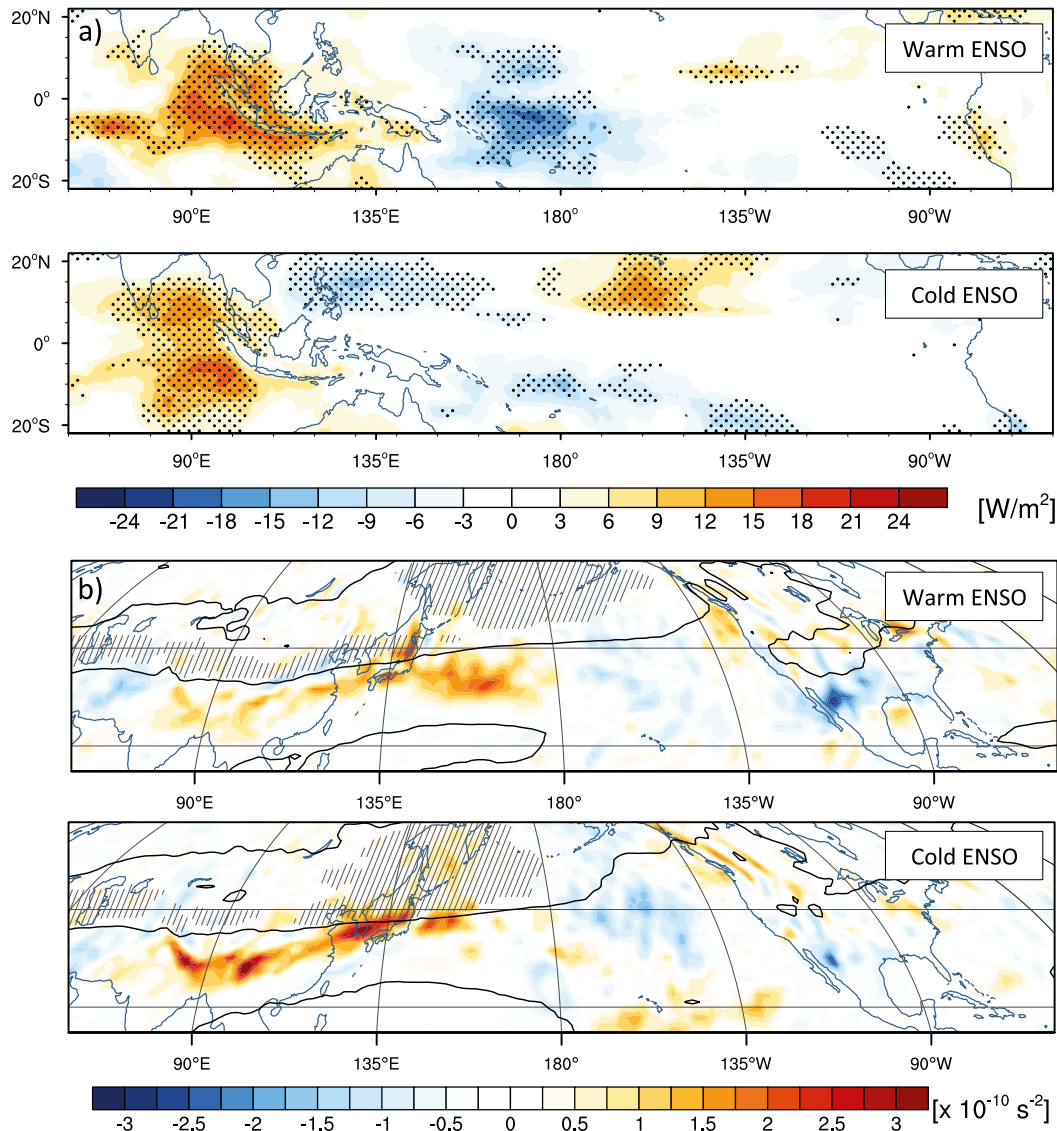


FIG. 5. RMM phase 7 pentad composites of 30–70-day filtered (a) OLR during (top) warm and (bottom) cold ENSO, and (b) Rossby wave source (RWS; color shading) during (top) warm and (bottom) cold ENSO. In (a), dotted regions indicate OLR anomalies 95% significantly different from zero based on a two-tailed Student's  $t$  test. In (b), the  $K_s = 3$  contour line from Fig. 3 is overlaid and the  $\beta_M < 0$  regions are hatched north of 25°N.

from the Pacific over North America during pentads 0 and 1 (Fig. 8, left column). The Rossby waves lead to a dipole structure over northeast North America and Greenland (Fig. 8), which is not observed during La Niña (Fig. 9). The dipole structure persists through pentad 3, or approximately 15–19 days after RMM phase 7 (Fig. 8). The Atlantic pattern is similar to cluster 4 in Riddle et al. (2013, their Fig. 3), which they compare to a negative Arctic Oscillation (AO)-like pattern. In agreement with our results, the study noticed the increased occurrence of this pattern following RMM phase 7 during El Niño, and note that further work is

needed to understand why the increased frequency of the pattern exists.

## 5. MJO impacts on blocking during ENSO

The influence of the MJO on Pacific and Atlantic high-latitude blocking is examined following the same compositing technique and significance testing as in H16. The dichotomous blocking indices indicating the presence of a large-scale persistent block are first composited relative to ENSO phase to determine the mean ENSO DJF blocking frequency (Fig. 10, middle and

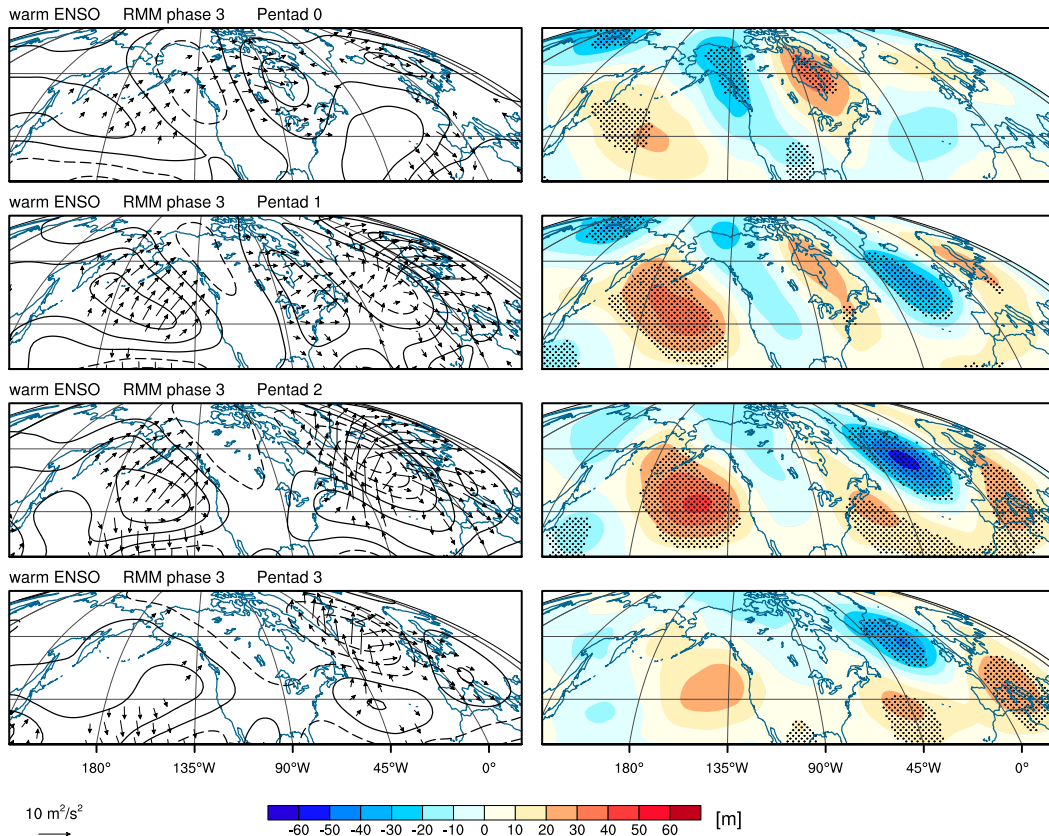


FIG. 6. Warm ENSO RMM phase 3 composites of 30–70-day filtered (left) 200-hPa streamfunction and (right) 500-hPa geopotential height for (top to bottom) pentad 0 to pentad 3, where a pentad is a 5-day mean. Black dotting demonstrates the anomalies found to be 95% significantly different from zero. Positive (negative) streamfunction is in solid (dashed) contours with an interval of  $15 \times 10^5 \text{ m}^2 \text{ s}^{-2}$ , and the zero contour is omitted. Overlaid on streamfunction are wave activity flux vectors. Vectors with a magnitude below  $2 \text{ m}^2 \text{ s}^{-2}$  are omitted. The reference vector is provided below the left column.

bottom panels). The blocking frequency maximum over the west-central Pacific is largely influenced by the meridional gradient of geopotential height, which is climatologically weak in that region (e.g., Woollings et al. 2008). During El Niño, this blocking frequency maximum has slightly higher amplitude than the DJF climatological mean (Fig. 10, top left panel) and neutral ENSO conditions (not shown). In contrast, the frequency of high-latitude Pacific blocking during La Niña is substantially reduced. As previously discussed, the high-latitude meridional gradient of geopotential height is strengthened by the anomalous anticyclonic response to La Niña tropical heating. Blocking as defined by (1) is associated with a reversal in the geopotential height gradient, which is harder to achieve at higher latitudes during La Niña. During El Niño, the cyclonic anomaly (Fig. 1) acts to weaken the high-latitude meridional gradient where it is already relatively weak, so that the impact is not as great. In contrast to the Pacific, when viewed in isolation ENSO has a lesser impact over the Atlantic (e.g., Fig. 1), and

changes to the mean blocking frequency are relatively small (Fig. 10, right column).

Blocking frequency anomalies composited relative to MJO and ENSO phase are shown in Figs. 11 and 12 for the Pacific and Atlantic, respectively, and are calculated by subtracting the DJF mean (Fig. 10, top panels) from each composite. The blocking frequencies are lagged relative to RMM phase, as indicated on the top left of each panel, where an  $m$ -day lag is the blocking frequency  $m$  days after that RMM phase. Dotted regions indicate that the blocking frequency anomalies are significantly different from zero at the 95% significance level using a moving-blocks bootstrap test, also used in H16. The moving-blocks bootstrap is calculated independently for each lag, MJO, and ENSO phase. Similar to a traditional bootstrap, the test approximates the data characteristics by sampling the data randomly, with replacement; however, the samples are taken in overlapping blocks of length  $l$  in order to preserve the data autocorrelation (e.g., Wilks 2011).

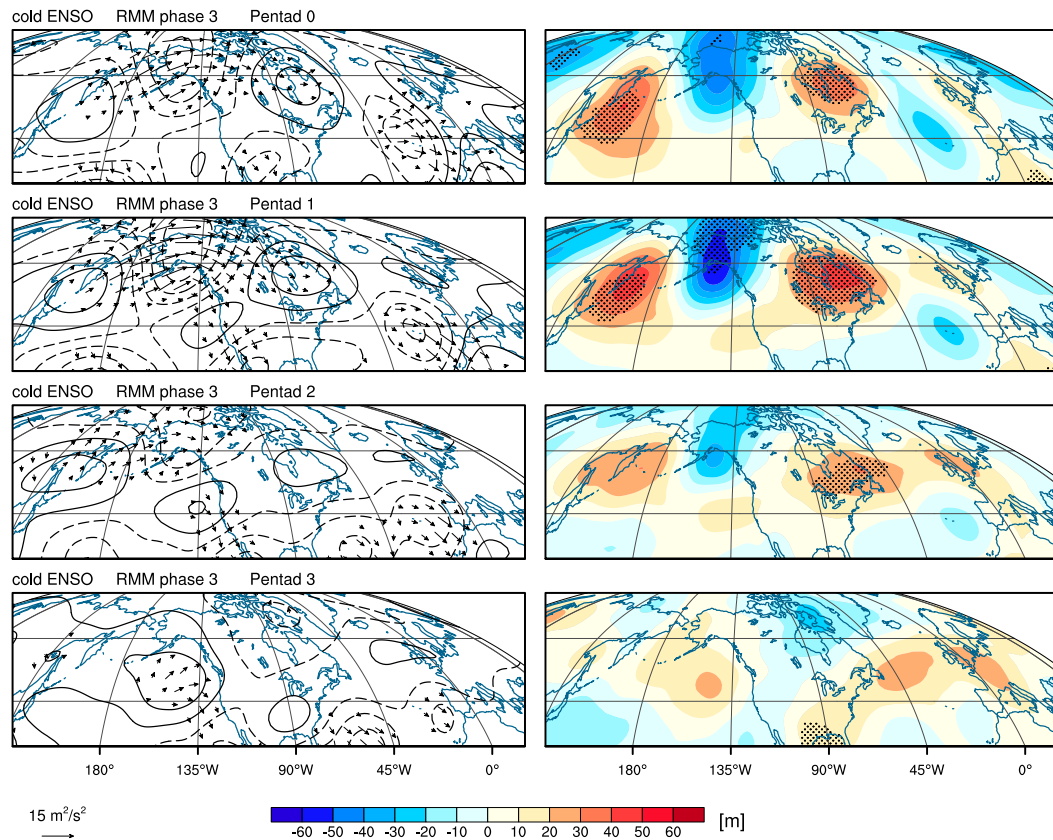


FIG. 7. As in Fig. 6, but for cold ENSO conditions.

The sampled blocks of length  $l$  are joined together to create bootstrap samples of size  $N$ , and the process is repeated 5000 times. Values of  $N$  are provided above each panel in Figs. 11 and 12, where  $N$  is the total number of days in that MJO and ENSO phase. Block length  $l$  is the estimated duration of each RMM phase, as in H16, calculated for each ENSO phase. During El Niño, the block lengths are found to be  $l = 4, 5, 7, 6, 4, 5, 6,$  and  $6$  for RMM phases 1–8, respectively. During La Niña,  $l = 4, 6, 5, 5, 6, 5, 6,$  and  $5$  for phases 1–8, respectively. For a more detailed description of the moving-blocks bootstrap and block length calculation, see H16. Similar results were obtained using a more conservative block length that assumed all MJO events within the same ENSO season were fully dependent (not shown). Also shown in Figs. 11 and 12 are the number of days  $N_B$  in that MJO and ENSO phase that observed large-scale persistent blocking, and a ratio  $R = N_B/N$ , indicating the percent of days that experienced blocking  $m$  days after that RMM phase during an ENSO event. Note that  $N_B$  is a total count for the full basin including the blocking events that make up the DJF mean (i.e., Fig. 10).

The anomalous blocking frequency composites presented in this section are recreated using a longer

reanalysis dataset, spanning from 1949 to 2016, in the appendix as a way to address the sample size limitations introduced when compositing by ENSO and RMM phase. Although the longer timeline allows for more samples, data prior to the satellite-era have sparser observations and exclude satellite-derived fields such as OLR.

#### a. Pacific blocking

Based on the findings of H16, RMM phases 1–5 are associated with significant suppression in Pacific high-latitude blocking due to a strengthening of the meridional geopotential height gradient by the MJO teleconnection patterns. This blocking suppression shifts eastward with RMM phase as the MJO-induced geopotential height anomalies move eastward. This suppression is evident during ENSO neutral years (not shown); however, there are some key differences during cold and warm ENSO events. Pacific blocking anomalies during and following RMM phase 3 during warm and cold DJF seasons are shown in Figs. 11a and 11b (top rows), respectively. The neutral (not shown) and cold (Fig. 11b, top row) ENSO phases demonstrate a significant suppression in central Pacific blocking, whereas anomalies are not significant for warm ENSO events

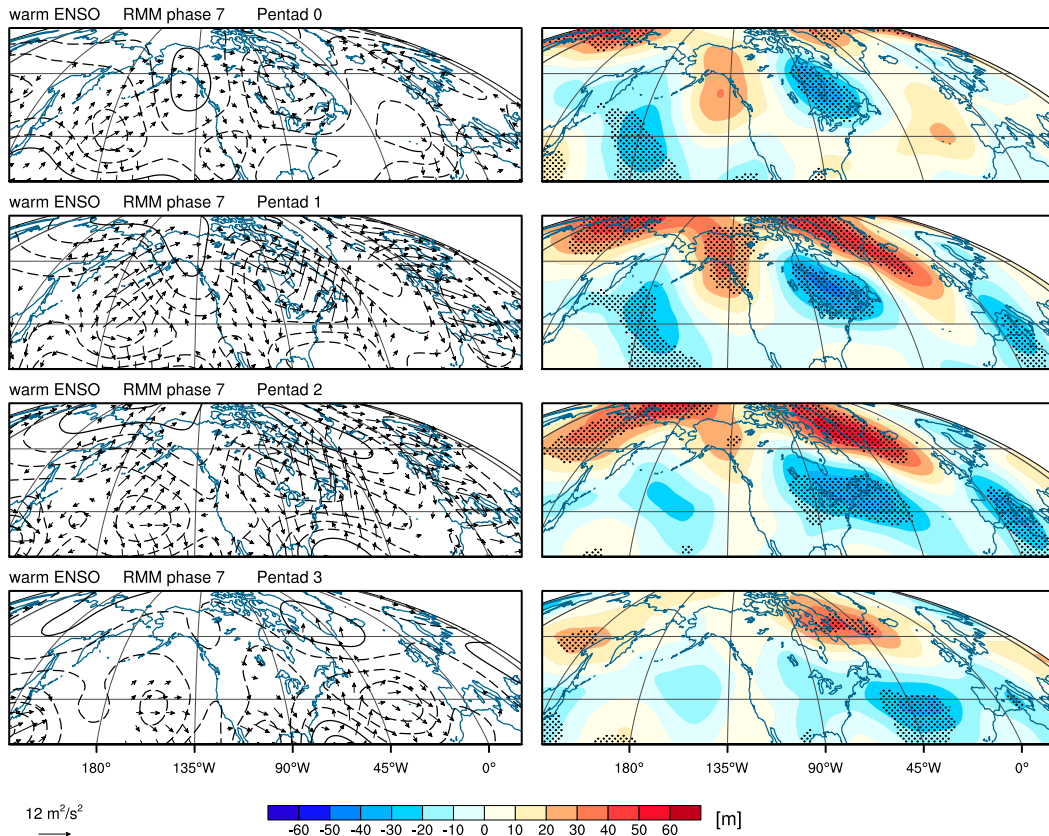


FIG. 8. As in Fig. 6, but for RMM phase 7.

(Fig. 11a, top row). In all lags investigated here, significant blocking anomalies are primarily observed in the latter half of the MJO cycle during El Niño and in the first half of the MJO cycle during La Niña. To understand why these differences exist, the combined impact of ENSO and MJO teleconnections is examined.

The unfiltered 500-hPa geopotential height anomalies for RMM phase 3 pentad 1 is shown in Fig. 13 for warm (top left) and cold (bottom left) ENSO phases. These unfiltered patterns are calculated by removing the long-term daily mean and the first three harmonics of the seasonal cycle and demonstrate the combined impact of ENSO and the MJO 5–9 days after RMM phase 3. During El Niño, the combined impact of ENSO and RMM phase 3 is relatively weak. This is because the negative Pacific geopotential height anomaly associated with El Niño (Fig. 1, top) is partially cancelled out by the significant positive geopotential height anomaly in the same region that follows RMM phase 3 (Fig. 6, second panel). These teleconnection patterns in the Pacific act destructively, and no significant changes in blocking occur. During La Niña, however, there is a strong anticyclonic anomaly over the east Pacific between 30° and 60°N (Fig. 1), while RMM phase 3 pentad 1 is associated with a cyclonic anomaly north of approximately

50°N (Fig. 7, second row). Combined, a strong dipole exists over the eastern half of the North Pacific basin (Fig. 13, bottom left). This dipole acts to strengthen the geopotential height gradient and blocking is significantly suppressed along the southern and western flanks of the cyclonic anomaly. For similar reasons, significant suppression of Pacific blocking is observed following RMM phases 1–5 during La Niña (only phase 3 shown).

The latter half of the MJO life cycle (RMM phases 6–8) is associated with the eastward propagation of a negative geopotential height anomaly near the subtropical jet and a positive geopotential height anomaly to its northeast (e.g., H16). This pattern is evident following RMM phase 7 for both ENSO phases (Figs. 8 and 9); however, the blocking impacts greatly differ between warm and cold ENSO conditions (Fig. 11; second and fourth row). During El Niño, a significant persistent increase in blocking occurs across the North Pacific, lasting from approximately 5 to 15 days after RMM phase 7 (Fig. 11a, bottom row). The persistent increase is reflected in other RMM phases, with a significant increase in blocking frequency following RMM phases 6–8 (only phase 7 shown). This significant increase in blocking frequency does not appear in the cold ENSO composites (Fig. 11b, bottom row).

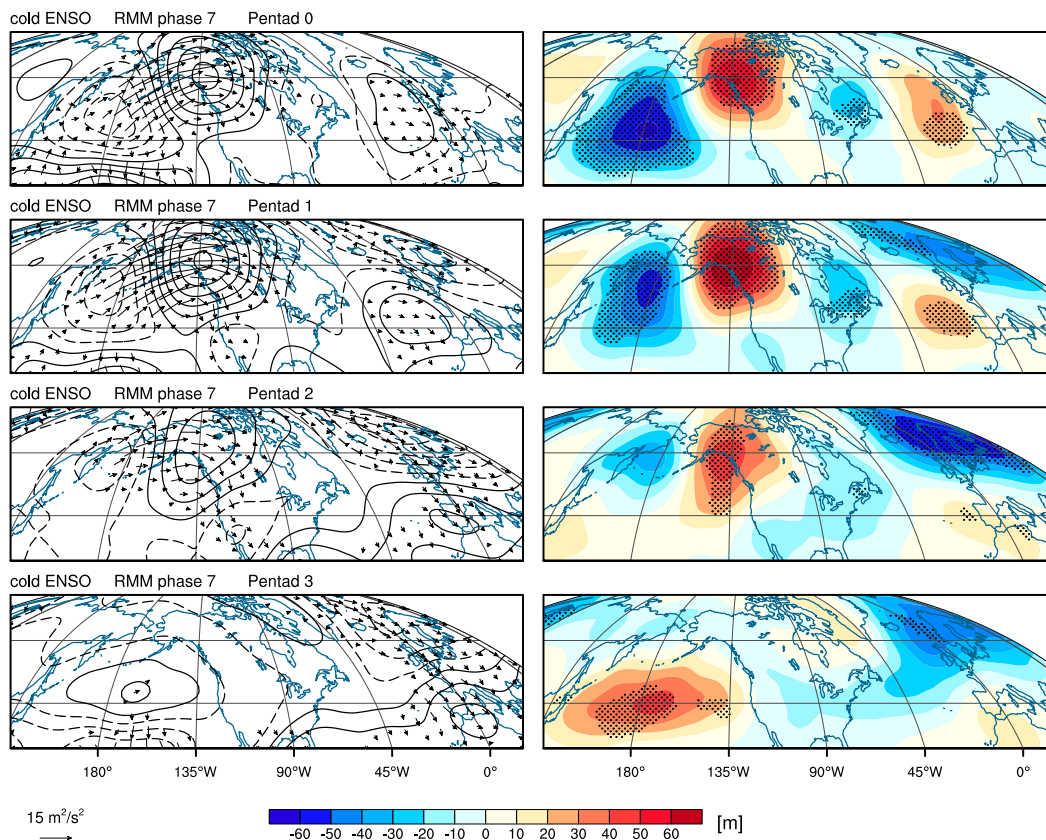


FIG. 9. As in Fig. 6, but for RMM phase 7 during cold ENSO conditions.

These differences can be better understood by examining the combined influence of ENSO and the MJO on the large-scale circulation. The unfiltered geopotential height anomalies following RMM phase 7 are shown in Fig. 13 (right column). Both El Niño (Fig. 1, top) and RMM phase 7, pentad 1 (Fig. 8, second row) are associated with anomalously negative geopotential height in the central Pacific, suggesting that the Rossby waves associated with both forms of variability will act constructively to amplify the anomaly in that region. The individual teleconnections (Figs. 1 and 8) suggest that the Pacific basin anomalies are only destructive in the Gulf of Alaska, as observed by the reduced southward extent of the positive geopotential height anomaly over northwest North America in Fig. 13 relative to Fig. 8. The negative central Pacific geopotential height anomaly is flanked by positive height anomalies to its north (Fig. 13, top right), indicating that there is a weakening of the mean meridional geopotential height gradient throughout the North Pacific basin so that a reversal, and hence a block as defined by (1), is easier to achieve.

During La Niña, Fig. 13 (bottom right) suggests that the anomalies west of the date line are relatively weak. The Pacific anticyclonic anomaly associated with La

Niña (Fig. 1, bottom) acts to extend the anticyclonic anomaly that follows RMM phase 7 (Fig. 9) southward, reaching approximately 30°N. The anticyclonic anomaly coincides with an increase in blocking frequency along western North America (not shown), indicating an impact on east Pacific midlatitude blocking. It is possible that the anomalous ridge over the northeast Pacific (Fig. 13) is associated with omega-type blocking that does not contain a reversal, which would be missed by the blocking index. Although the primary focus here is on high-latitude blocking, a brief examination of transient eddies during cold ENSO RMM phase 7 is discussed in section 5c, suggesting a possible impact on midlatitude blocking during this time.

#### b. Atlantic blocking

In the Atlantic basin, blocking is significantly suppressed following RMM phase 3 when considering all DJF seasons (e.g., H16; Hamill and Kiladis 2014), a relationship also observed during ENSO neutral years (not shown). Figure 12b (top row) indicates that Atlantic high-latitude blocking is suppressed following phase 3 during La Niña. During El Niño, suppressed regions that meet the significance criteria are less consistent between lags, suggesting a weaker relationship

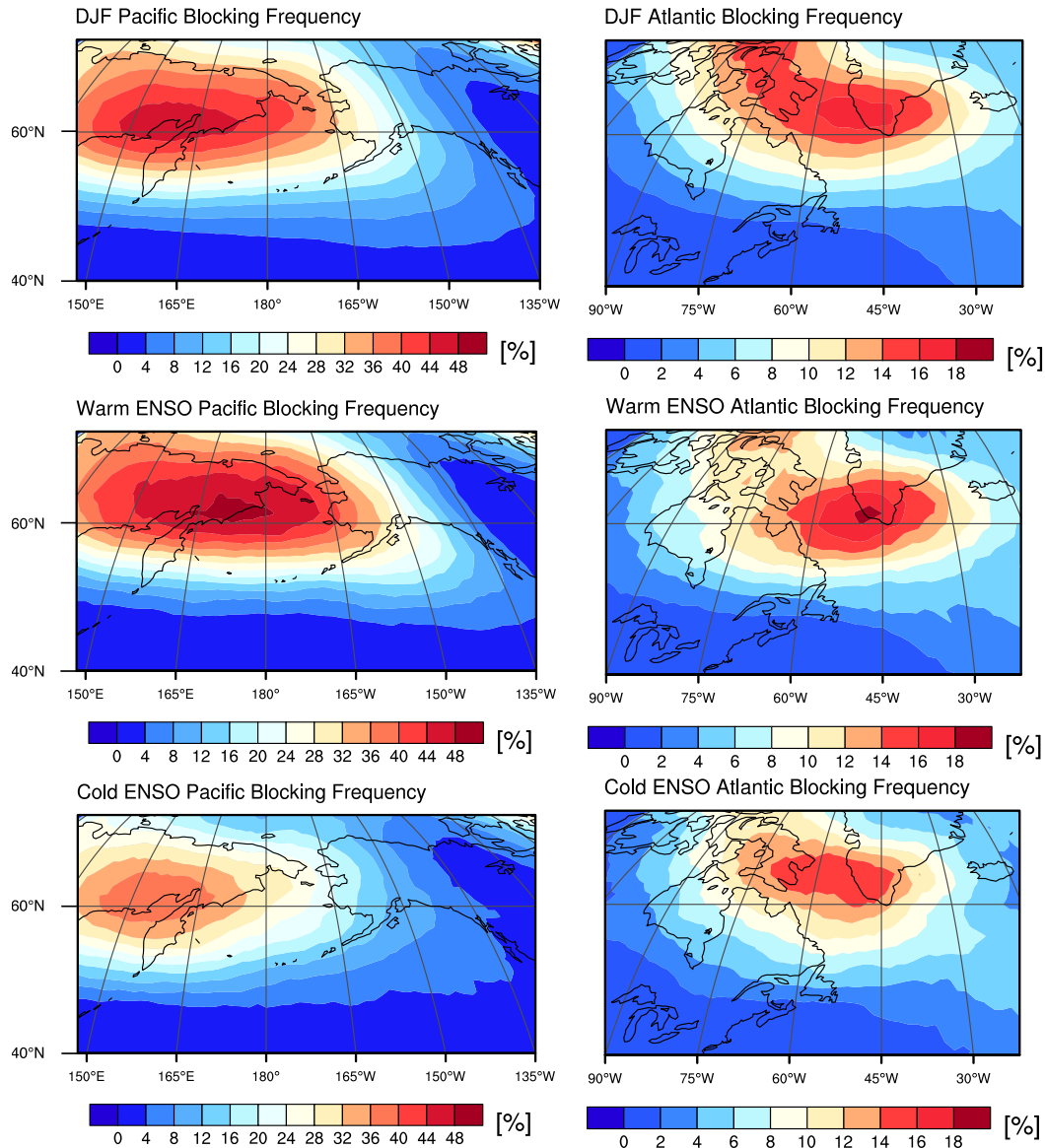


FIG. 10. Mean blocking frequency for the (left) Pacific and (right) Atlantic regions based on (top) all DJF seasons, (middle) warm ENSO DJF seasons, and (bottom) cold ENSO DJF seasons.

between the MJO and blocking (Fig. 12a, top row). In addition, suppressed regions are of weaker amplitude during El Niño; however, there is a large difference in sample size that can impact the relative amplitude of the anomalies (see  $N$  values above each panel). Filtered MJO teleconnection patterns demonstrate that a deep Atlantic trough follows RMM phase 3 during El Niño (Fig. 6), whereas during La Niña there is a significant ridge over northeast North America (Fig. 7). When considering both ENSO and the MJO, a trough emerges over Greenland during La Niña at pentad 1 (Fig. 13, bottom left). During pentads 2 and 3 (not shown), the ridge over northeast North America strengthens and

shifts slightly south with increasingly negative geopotential height anomalies to its north. This pattern suggests that following RMM phase 3 there is a persistent strengthening of the geopotential height gradient during La Niña that coincides with the reduced frequency of Atlantic high-latitude blocking (Fig. 12b, top row). During El Niño, the Atlantic trough (Fig. 13, top left) shifts east over northern Europe during pentad 2, weakening by pentad 3 (not shown), and the anomalous ridge over northeast North America (Fig. 13, top left) weakens substantially by pentads 2 and 3 (not shown). Atlantic blocking north of this anomalous ridge may be reduced in individual cases where the ridge is allowed to persist.

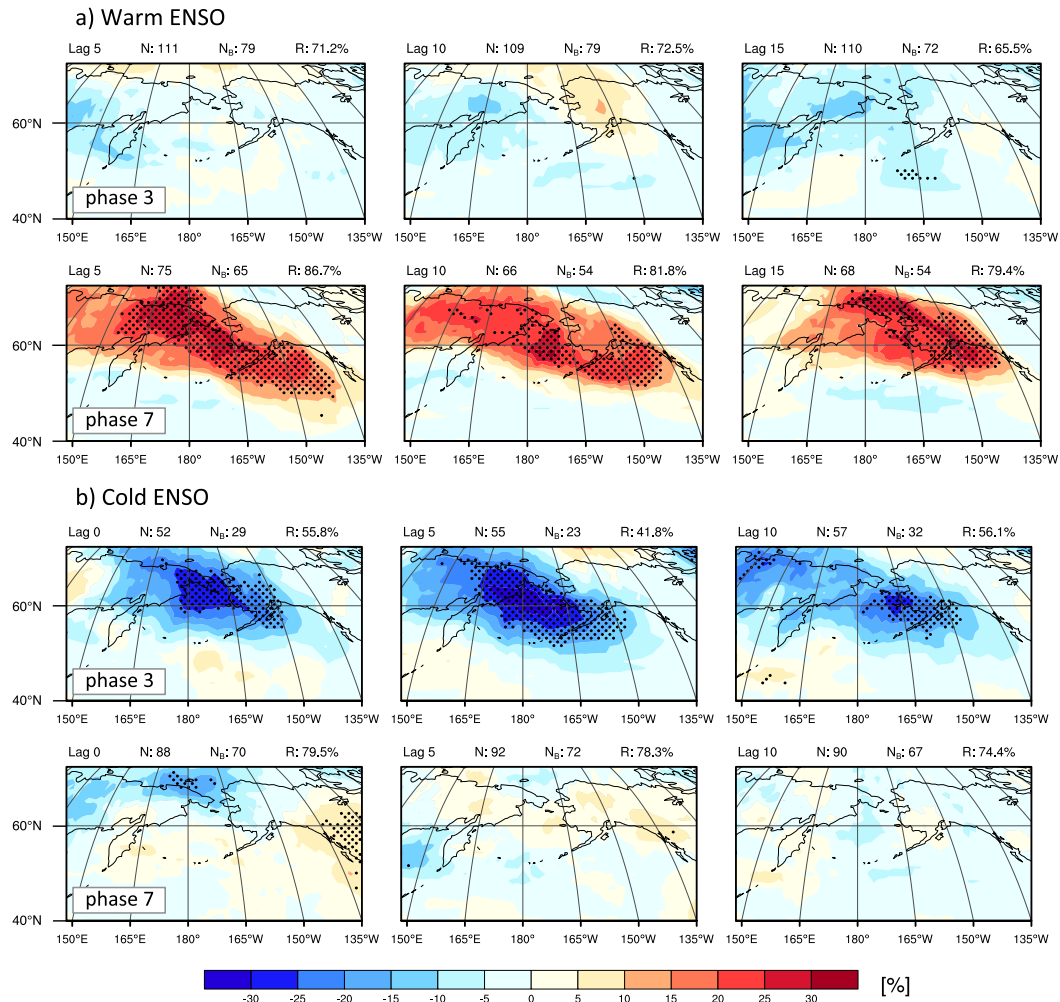


FIG. 11. Pacific blocking frequency anomalies during (a) warm and (b) cold ENSO conditions, with (a) showing frequency anomalies (left) 5, (center) 10, and (right) 15 days after RMM phases (top) 3 and (bottom) 7, and (b) showing anomalies at lags of 0, 5, and 10 days relative to the RMM (top) phase 3 and (bottom) phase 7. Anomalies are a deviation from the DJF mean (Fig. 10, top row). Black dotting indicates anomalies found to be 95% significantly different from zero. For explanation of the values above each panel, see section 5.

During El Niño, a significant increase in Atlantic blocking frequency is observed during and following RMM phase 7 (Fig. 12a, bottom row; lag 0 not shown), with maximum anomalies tripling that of the DJF mean (Fig. 10) at later lags. A significant increase in Atlantic blocking was also observed in H16 when considering all DJF seasons; however, the increase in blocking following phase 7 is not significantly different from zero when considering only ENSO neutral years (not shown) and only significant in a small region at later lags during La Niña (Fig. 12b, bottom row). This suggests that the inclusion of El Niño years was largely driving the significant Atlantic blocking increase discussed in H16. The intraseasonal teleconnection patterns associated with RMM phase 7 (Figs. 8 and 9) show a large difference in the Atlantic basin between the two ENSO phases. The persistent dipole

pattern in Fig. 8 is likely in part due to the increase in blocking, given the quasi-stationarity of the anomalies and the large percentage of blocking days that follows phase 7 during El Niño ( $R = \sim 73\%$  of days at lags 5 and 10; Fig. 12a, bottom row). One possibility is that the MJO initially provides the dipole anomaly and transient eddies act to reinforce and maintain the blocking pattern. The role of MJO heating on the development of the dipole anomaly will be investigated using the NBLM in section 6, and the role of transient eddies will be discussed next.

### c. The role of eddies in RMM phase 7 blocking anomalies

The persistence and quasi-stationarity of blocking patterns cannot be fully explained by MJO stationary waves since the MJO may evolve into the next phase

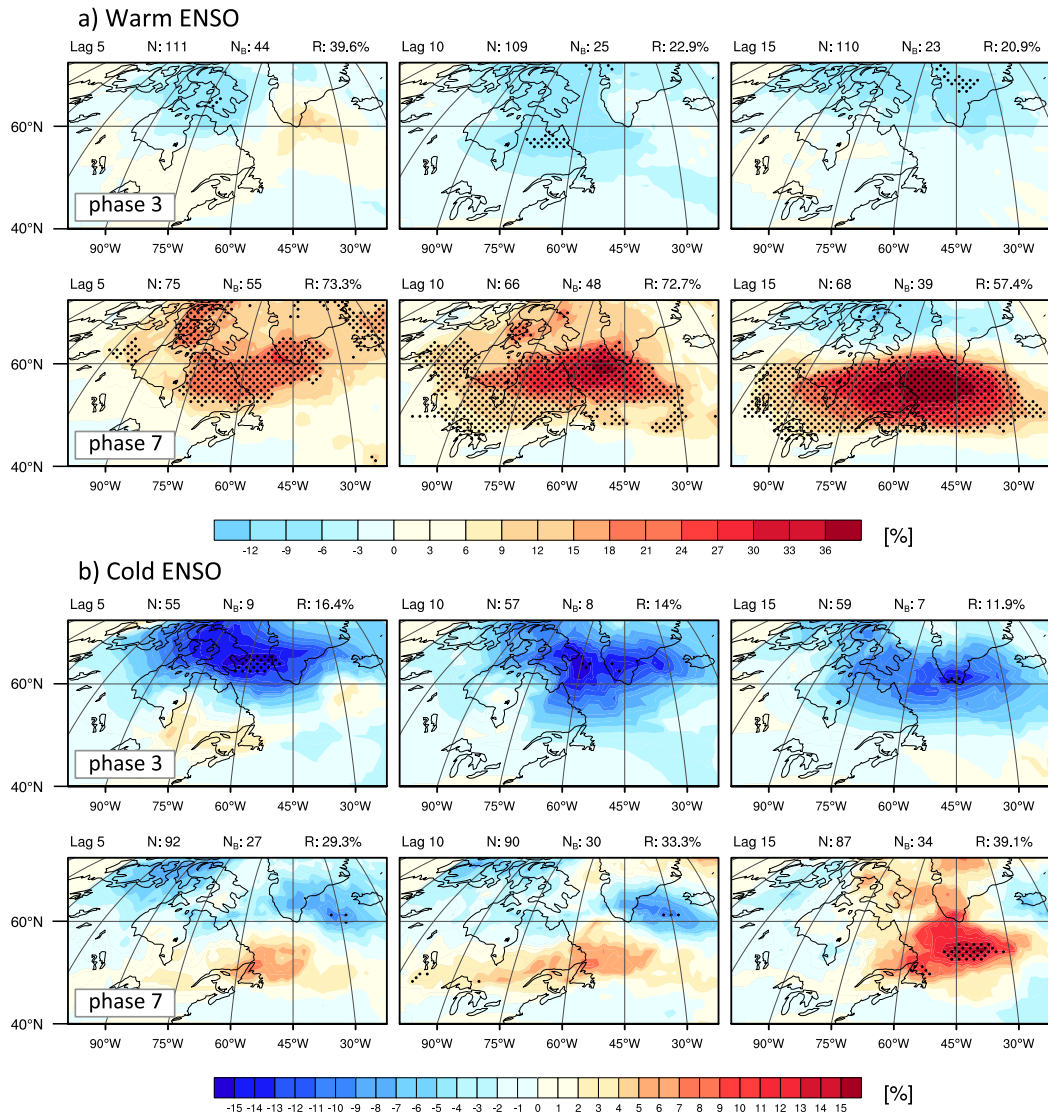


FIG. 12. Atlantic blocking frequency anomalies relative to the DJF mean during (a) warm and (b) cold ENSO conditions (left to right) 5, 10, and 15 days after RMM (top) phase 3 and (bottom) phase 7. Black dotting indicates anomalies found to be 95% significantly different from zero. For explanation of the values above each panel, see section 5.

with a time scale much shorter than the longevity of a block. Green (1977) found that eddies traveling along the storm track helped maintain the blocking pattern examined in their study by transporting low potential vorticity (PV), or anticyclonic vorticity, into the block. To better understand the role of eddies in maintaining blocking in association with MJO events, the horizontal **E** vector is used as formulated by Trenberth (1986):

$$\mathbf{E} = \left[ \frac{1}{2}(\overline{v'^2} - \overline{u'^2}), -\overline{u'v'} \right] \cos \theta, \quad (6)$$

where  $u$  and  $v$  are the 300-hPa zonal and meridional winds, respectively, and  $\theta$  is latitude. The primes indicate

a 2–6-day bandpass filter and the overbar a time mean. The **E** vector as defined by (6) examines the transport of angular momentum by transient eddies, where its convergence indicates the eddy activity acts to decelerate the local mean westerly wind, thereby reinforcing the block (Trenberth 1986). Here we examine the **E** vectors associated with RMM phase 7 during El Niño, which is associated with enhanced and persistent blocking (Fig. 12a).

Atlantic **E** vectors for phase 7 during El Niño are shown in Fig. 14, as well as the corresponding **E**-vector divergence (color shading). Also overlaid is the associated mean 300-hPa transient eddy kinetic energy [TEKE = (1/2)( $u' + v'$ )<sup>2</sup>], which estimates the location

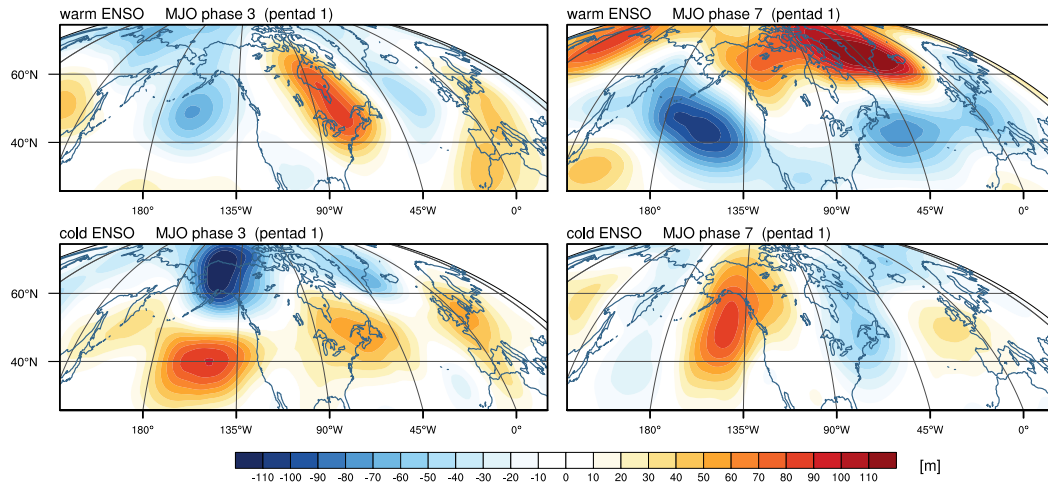


FIG. 13. RMM (left) phase 3 and (right) phase 7 pentad 1 composites of unfiltered 500-hPa geopotential height anomalies during (top) warm and (bottom) cold ENSO conditions.

of the storm track (e.g., Pelly and Hoskins 2003). The **E**-vector fields are smoothed by lowering the wind data resolution to a  $2.5^\circ$  grid prior to the **E**-vector calculation. The anomalous Atlantic pattern is observed during (Fig. 8, pentad 0) and following RMM phase 7 (pentads 1–3). We therefore examine eddy activity during (Fig. 14, left panel) and 10 days after phase 7 (right panel), in which approximately 73% of days contain a large-scale block largely concentrated south of Greenland and over the Labrador Sea (Fig. 12a, bottom row).

During RMM phase 7, **E**-vector convergence south of Greenland indicates that eddy activity is acting to decelerate the westerly flow near the center of and in the northern portion of the storm track (Fig. 14). The deceleration of the flow coincides with the initial increase

in Greenland blocking frequency (lag 0 not shown in Fig. 12a). The **E**-vector convergence is also observed along the northern flank of the storm track at lag 10 (Fig. 14, right panel). In the presence of an anticyclone, the deceleration of the flow suggests eddy activity acts to reinforce blocking activity by depositing low PV air into the block. During and following RMM phase 7, eddy activity accelerates the westerly flow along the southern flank of the storm track, indicated by **E**-vector divergence. This suggests that eddy activity acts to shift the storm track southward (see TEKE contours, lag 10), a characteristic commonly associated with Greenland blocking (e.g., Woollings et al. 2008).

In section 5a, we discussed an anomalous ridge over the northeast Pacific that may be associated with omega-type

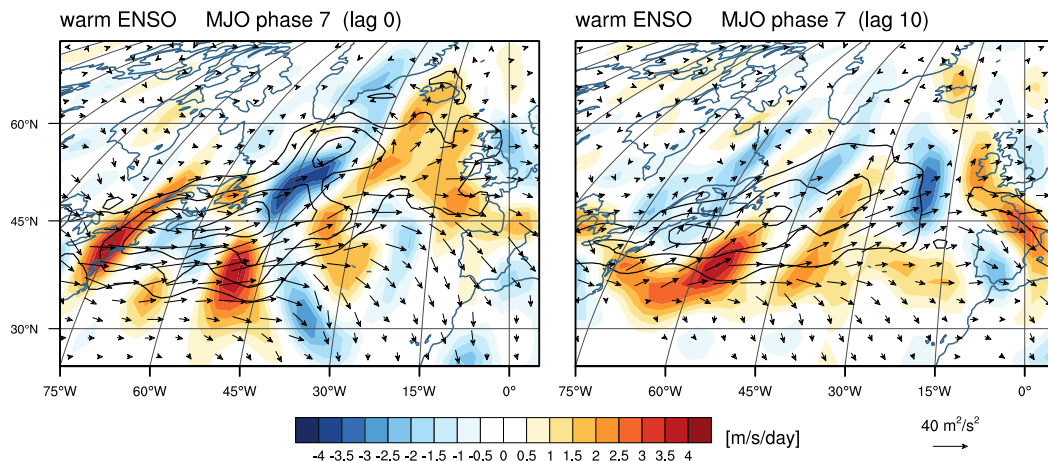


FIG. 14. Warm ENSO composites of 300-hPa mean transient eddy kinetic energy (TEKE; contours), **E** vectors, and **E**-vector divergence (color shading) during (left) lag 0 and (right) 10 days after RMM phase 7. The TEKE contour interval is  $20 \text{ m}^2 \text{ s}^{-2}$  beginning at  $90 \text{ m}^2 \text{ s}^{-2}$ . **E** vectors of magnitude less than  $5 \text{ m}^2 \text{ s}^{-2}$  are omitted.

blocking. Although midlatitude blocking is beyond the scope of this paper, here we briefly discuss the behavior of east Pacific transient eddies during cold ENSO RMM phase 7. Composites of  $\mathbf{E}$ -vector divergence and TEKE during RMM phase 7 suggest that TEKE is reduced relative to mean cold ENSO conditions (not shown). There is  $\mathbf{E}$ -vector convergence near the center of the anomalous east Pacific ridge (see Fig. 13), extending from the Alaskan southern coast to approximately 40°N (now shown). This suggests that transient eddies are acting to slow the westerly flow in this region, thereby reinforcing possible blocking conditions. The  $\mathbf{E}$ -vector convergence persists through lag 10, and is followed by a strengthening of the storm track at later lags. MJO influence on east Pacific omega-type midlatitude blocking necessitates further investigation and is a subject of future work.

This  $\mathbf{E}$ -vector analysis provides some understanding of the maintenance and persistence of the blocking pattern shown in Figs. 8 and 12a. While  $\mathbf{W}$  vectors suggest that MJO Rossby wave propagation is involved in the development of the dipole anomaly (Fig. 8), a cause and effect argument is difficult because composite analysis does not distinguish between the geopotential height anomalies generated by the significant increase in blocking and the anomalies generated by the MJO Rossby waves. To better understand the role of the MJO on the dipole anomaly, a simple nonlinear model is employed.

## 6. NLBM experiments

The impact of the MJO on the atmospheric circulation during ENSO events is investigated using the nonlinear dry baroclinic model introduced by Yasui and Watanabe (2010). The NLBM is a simplified dry atmospheric general circulation model derived from primitive equations on a sphere, and has been used by various studies to examine the nonlinear response to anomalous forcing (e.g., Nakamura et al. 2015; Kosaka et al. 2012). The NLBM is first used to examine the differences between the RMM phase 3 teleconnection patterns for different ENSO phases, and help determine if these changes are primarily explained by the ENSO-induced differences in basic state and MJO heating rather than an effect of the blocking anomalies themselves. RMM phase 3 also demonstrates the greatest difference in sample size between cold and warm ENSO events. Recreating the phase 3 teleconnection patterns using the NLBM helps to ensure that the teleconnection pattern composites are not substantially impacted by these differences in sample size (also see the appendix). In addition, the model is used to examine the role of the MJO on the phase 7

Atlantic blocking pattern discussed in the previous section.

### a. NLBM description and setup

The NLBM calculates the nonlinear response to a prescribed forcing given a user-specified basic state. In the NLBM, the basic state can be thought of as the initial condition of the model that is perturbed only by the prescribed forcing. The model has a T42 horizontal resolution and 20 vertical levels on  $\sigma$  surfaces. It employs biharmonic diffusion with an  $e$ -folding time scale of 1 day for the largest wavenumbers. The prescribed basic state is maintained by nudging temperature back toward the basic state every 10 days using Newtonian cooling (e.g., Nakamura et al. 2015). The experiments are ran for 50 days and include two control runs and the MJO-forcing runs. The two control runs are initialized with the DJF El Niño and La Niña basic state, respectively, calculated from ERA-Interim 1979–2016 data. The MJO-forcing runs are prescribed an ENSO basic state and initialized using a propagating MJO heat source, discussed below. The anomalous response to MJO heating is then the difference between the MJO-forced run and the control run of the same ENSO basic state.

The apparent heat source ( $Q_1$ ; Yanai et al. 1973) anomaly associated with the MJO during a given ENSO phase is used to force the NLBM. The value of  $Q_1$  is calculated using DJF ERA-Interim reanalysis data from 1979–2016 as a residual of the dry static energy ( $s$ ) budget, given by

$$Q_1 = \frac{\partial s}{\partial t} + \nabla \cdot (s\mathbf{V}) + \frac{\partial(s\omega)}{\partial p}, \quad (7)$$

where  $s = c_p T + gz$ , in which  $c_p$  is the specific heat capacity of air at constant pressure,  $T$  is the temperature,  $g$  is the gravitational constant, and  $z$  is the height. In (7),  $\omega$  is the pressure velocity and  $\mathbf{V}$  is the horizontal wind vector. Anomalies in apparent heating ( $Q_1$ ) are calculated by applying a 30–70-day bandpass filter to remove diabatic heating anomalies associated with ENSO and other types of variability, and compositing by MJO and ENSO phase. For each ENSO phase, a 48-day propagating heat source is derived by using the eight MJO  $Q_1$  phase composites and linearly interpolating, under the assumption that each RMM phase spans approximately 6 days. The idealized 48-day MJO cycle was also used in Henderson et al. (2017), which used a propagating heat source to force the linear version of the model used here (LBM; Watanabe and Kimoto 2000).

For each MJO forcing run, it is important to consider what RMM phase will begin each 48-day cycle. It is

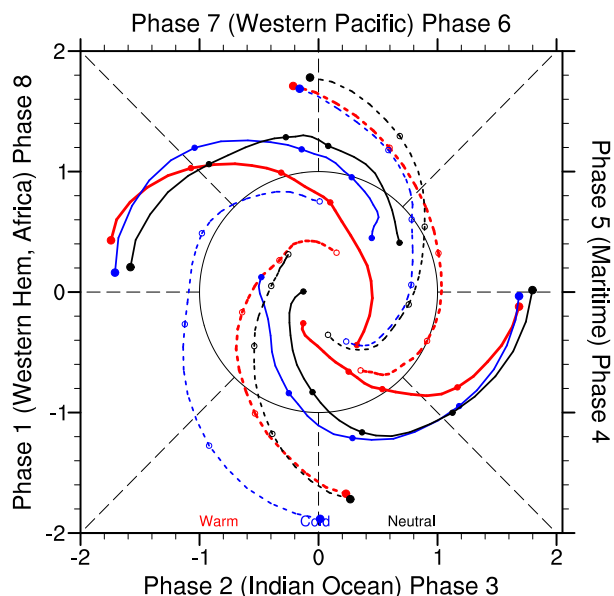


FIG. 15. RMM index amplitude backward trajectories in phase space during the warm (red), cold (blue), and neutral (black) ENSO phases. Trajectories initiate in each quadrant when the ENSO phase RMM index indicates a strong amplitude MJO event ( $>1.3$ ) in phases (bottom) 2-3, (right) 4-5, (top) 6-7, and (left) 8 or 1. Each trajectory is shown for 21 days (20 days prior to initiation). Circles mark every 5 days. The composite indices are smoothed using a 5-point running mean prior to plotting (e.g., Rashid et al. 2011).

possible that the teleconnection patterns during a given RMM phase is influenced by many RMM phases before it, although the evolution of MJO events are often more episodic than continuous. The average MJO evolution during ENSO events is examined using the two-dimensional RMM phase space (Fig. 15), where the  $x$  and  $y$  axes are RMM1 and RMM2, respectively. A typical strong MJO event is characterized by counterclockwise motion in the RMM phase space and an amplitude greater than 1, indicated by the unit circle in the figure. Average MJO persistence is calculated in a similar way as in Rashid et al. (2011) and Henderson et al. (2017), which computed the average phase-space trajectory and decay time scale (i.e., the moment in which the trajectory falls below the unit circle) of strong MJO events beginning at each phase-space quadrant. However, we calculate these trajectories backward in time (i.e., clockwise motion in phase space) since we are interested in determining which RMM phase in which to begin each 48-day  $Q'_1$  forcing.

The initial point of each trajectory, marked by a large filled circle in Fig. 15, is the average RMM value for strong MJO events in each phase quadrant during El Niño (red) and La Niña (blue). For reference, trajectories during neutral years are also provided in black. The

backward trajectories are initialized in RMM phases 2–3 (Fig. 15, bottom quadrant), 4–5 (right quadrant), 6–7 (top quadrant), and 8–1 (left quadrant), with alternating dashed and solid curves for clarity. Here we focus on the backward trajectories initialized in RMM phases 2–3 and phases 6–7 since we are interested in the phase 3 and phase 7 teleconnection patterns. The RMM phase in which the trajectories fall below the unit circle is then the average phase that an MJO event begins with that leads to strong RMM phases 2–3 or 6–7. Figure 15 suggests that MJO events persist very differently depending on ENSO and RMM phase. For example, a strong RMM phase 2–3 during La Niña is preceded on average by relatively persistent MJO activity beginning in the previous MJO cycle. During El Niño and neutral conditions, however, the trajectory does not extend beyond one RMM phase. MJO persistence also varies by ENSO phase for the RMM phase 6–7 trajectories. During El Niño, more persistent MJO activity precedes a strong RMM phase 6–7 than during La Niña, with an initial phase 4 during El Niño. Figure 15 provides a useful guide on what preceding RMM phase to initiate the propagating heat source in the NLBM experiments in order to determine heating anomalies during a target phase.

#### b. NLBM experiments: Phase 3 teleconnection patterns

This section will use the NLBM to examine the RMM phase 3 differences as a function of ENSO phase. The propagating  $Q'_1$  for the El Niño run is initiated using RMM phase 2, whereas the La Niña run is initiated using RMM phase 8. These initialization phases provided the results most comparable to Figs. 6 and 7. Figure 16 (top panel) shows the El Niño 500-hPa geopotential height NLBM response to MJO heating averaged from 21 to 26 days after initialization of the run, or 14 to 19 days after RMM phase 3 begins. Figure 16 (bottom panel) is the response to MJO heating using a La Niña basic state, and is shown as the average from days 25–30 after initialization of the run, or approximately 7 to 12 days after phase 3 begins. This earlier time frame is shown since the significant anomalies that follow RMM phase 3 during La Niña are largely confined to the earlier MJO lagged pentads (Fig. 7).

The NLBM response using the El Niño basic state and MJO heating (Fig. 16, top) shows many similarities to the composites following RMM phase 3, particularly pentads 1–2 (Fig. 6, second and third rows). In agreement with Fig. 6, the NLBM response has an anticyclonic anomaly over the east Pacific and a meridionally elongated cyclonic anomaly over western North America. Relative to the La Niña NLBM run

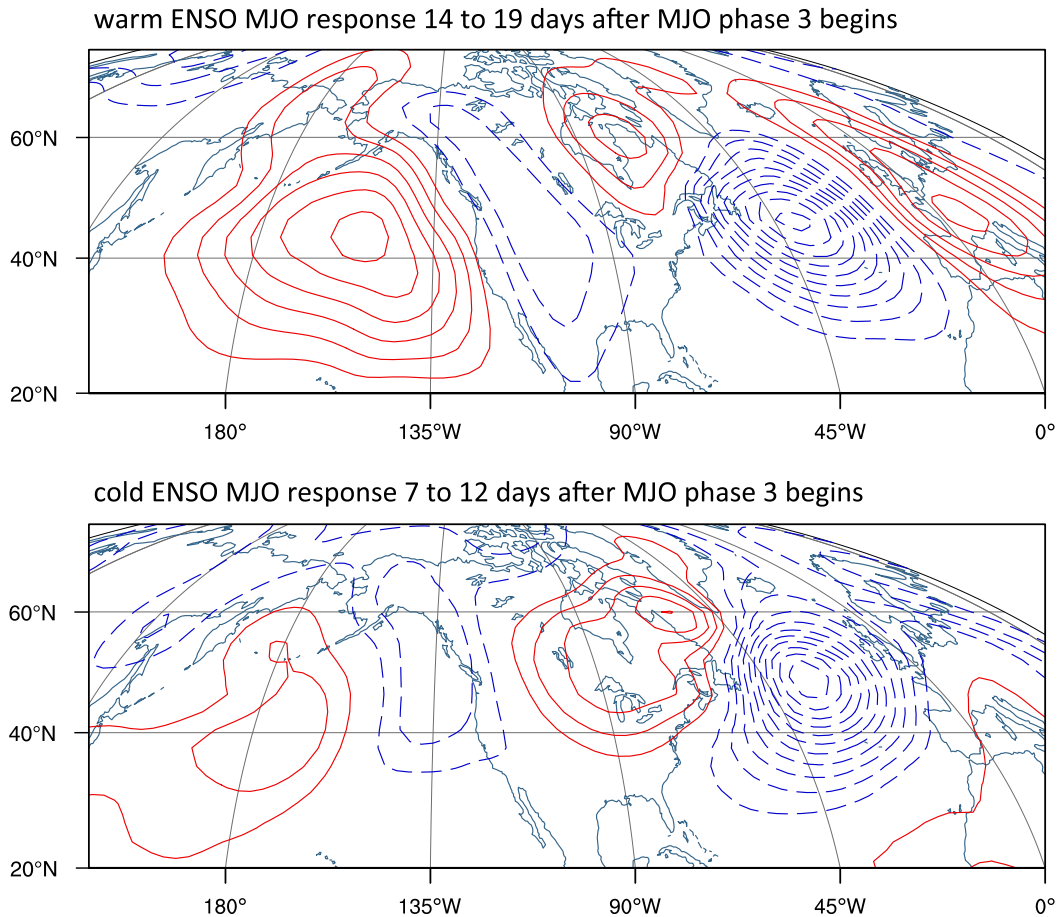


FIG. 16. NLBM 500-hPa geopotential height anomaly response against the (top) warm and (bottom) cold ENSO basic state. The warm ENSO run is the average 21–26-day response to a propagating heat source initiated with RMM phase 2 heating, and corresponds to 14–19 days after RMM phase 3 begins. The cold ENSO run is the average 25–30-day response to a propagating heat source initiated with RMM phase 8 heating and corresponds to 7–12 days after RMM phase 3 begins. See text for further details regarding the propagating heat source used. Contours are every 5 m and the zero contour is omitted.

(Fig. 16, bottom), the El Niño Pacific anomalies are shifted east in agreement with our previous discussion. In the La Niña NLBM run, the anticyclonic anomaly forms and maintains west of 150°W with the cyclonic anomaly over the east Pacific, in agreement with Fig. 7, pentads 0–1 (first two rows). The shift demonstrated here is similar to the LBM results of Henderson et al. (2017), who found an eastward shift in the Pacific MJO teleconnection patterns in GCMs with a zonally extended subtropical jet such as that observed during El Niño (e.g., Fig. 2). In addition, the La Niña NLBM run suggests that the Pacific geopotential height anomalies (Fig. 7) are not caused by the significant suppression of blocking (Fig. 11b, top row) since blocking is not simulated in this simple model. However, it is possible that the blocking anomalies amplify the geopotential height anomalies.

In the El Niño run (Fig. 16, top), a deep trough develops over the Atlantic and an anticyclonic anomaly over Europe. A similar pattern is also observed in the pentads following RMM phase 3 (Fig. 6), with the NLBM deep trough shifted south relative to reanalysis. In the La Niña run, the NLBM is able to capture the anticyclonic anomaly over northeast North America previously discussed to aid in the suppression of Atlantic high-latitude blocking that follows RMM phase 3, suggesting the geopotential height anomaly is forced by MJO heating and not due to the suppression of blocking itself. However, the NLBM extends the anticyclonic anomaly too far northeast relative to the composite. Furthermore, the NLBM strengthens the Atlantic cyclonic anomaly (Fig. 16, bottom) whereas the composite does not (Fig. 7). It is possible that the cyclonic anomaly is suppressed by internal variability or an external forcing

outside of the MJO, which would not be captured by the NLBM.

### *c. NLBM experiments: Phase 7 El Niño pattern*

The role of MJO Rossby waves in producing the RMM phase 7 El Niño Atlantic dipole (Fig. 8) is examined using a propagating heat source beginning with RMM phase 4 in conjunction with the El Niño basic state. Since the significant Atlantic cyclonic anomaly is observed during RMM phase 7 (Fig. 8, top row), we show the NLBM response prior to (Fig. 17, top), during (middle), and following (bottom) phase 7. The cyclonic anomaly over northeast North America develops prior to phase 7 (top) and grows during phase 7 with an anticyclonic anomaly to its north (middle). Whereas Fig. 8 demonstrates that the dipole anomaly persists, the dipole does not persist in the NLBM. Rather, the cyclonic anomaly propagates eastward (Fig. 17, bottom) and the anticyclonic anomaly dissipates. This is not surprising since the NLBM lacks dynamics important for blocking maintenance, such as eddy–mean flow interactions. Figure 17 suggests that MJO Rossby waves can develop an Atlantic dipole anomaly such as that observed in Fig. 8 that can act as the initial impetus for blocking anomalies. The blocking pattern can then be maintained by non-MJO dynamics, such as that discussed in section 5c.

## 7. Summary and discussion

The influence of MJO teleconnections during ENSO events on high-latitude blocking is examined, expanding on the results discussed in H16. Results demonstrate that during El Niño, MJO Pacific teleconnection patterns are shifted east relative to La Niña. During RMM phase 3, the Pacific teleconnection patterns associated with the MJO and El Niño are largely destructive, producing little impact on high-latitude blocking. Conversely, during La Niña the RMM phase 3 Pacific teleconnection pattern anomalies are largely constructive, and blocking is significantly suppressed throughout the North Pacific. Experiments using the NLBM demonstrate that the phase 3 La Niña teleconnection pattern is largely explained by MJO heating and the La Niña basic state, suggesting that the geopotential height anomalies during phase 3 are not a result of the significant suppression of blocking but rather Rossby wave teleconnections forced by the MJO. However, the blocking anomalies may amplify the geopotential height anomalies. Furthermore, the RMM phase 7 Pacific teleconnections during El Niño add constructively to the El Niño teleconnection pattern and are associated with a significant and persistent increase in blocking frequency.

During La Niña, the phase 7 Pacific teleconnection pattern does not destructively interfere with the La Niña teleconnection pattern, but it produces a pattern not favorable for west Pacific high-latitude blocking. It may, however, be associated with east Pacific midlatitude blocking and necessitates further investigation.

The El Niño phase 7 teleconnection pattern is associated with a significant and persistent increase in Atlantic blocking, with local blocking frequencies reaching 3 times those of the DJF mean. Atlantic phase 7 blocking frequency anomalies are not significant during neutral ENSO, suggesting that the significant increase during El Niño largely accounts for the near doubling in blocking frequency discussed in H16. Results using an NLBM indicate that MJO Rossby waves provide the initial dipole anomaly observed during RMM phase 7. The blocking pattern is then likely maintained by transient eddy activity.

The investigations in this study are limited by the sample sizes of each MJO and ENSO phase, which is in part taken into account by the use of the NLBM as well as examining the blocking composites using the longer NNR1 dataset (see the appendix). However, caution is necessary when comparing the amplitude of the composites due to differences in RMM phase sample size between ENSO phases. Future work includes examining the results discussed here using long-term GCM simulations, which diminish the impact of sample size limitations. Furthermore, important factors for the MJO–blocking relationship, such as the background flow and transient eddy activity, evolve with the seasonal cycle. This suggests that results for each individual month will likely have some differences from the seasonal composites discussed here. Results would also vary depending on ENSO amplitude and type (e.g., east Pacific vs central Pacific ENSO), requiring further investigation. Additionally, the NLBM has limitations due to its simplicity. MJO teleconnections may involve feedbacks with latent heat release in the mid-latitudes, as well as interactions with the mean flow and synoptic activity (e.g., Sakaeda and Roundy 2014; Roundy et al. 2017). These relationships would not be captured by the NLBM and may account for some of the differences from reanalysis.

In addition to the impact of ENSO on MJO teleconnections, which is the primary focus here, the MJO can influence ENSO teleconnections. For example, Hoell et al. (2014) found that MJO activity can amplify or weaken the magnitude of the ENSO teleconnection patterns by altering ENSO precipitation. This, in turn, can impact atmospheric blocking frequency and compels further investigation. In addition, MJO teleconnections during ENSO events may influence midlatitude blocking over the east Pacific and Europe. These regions have a

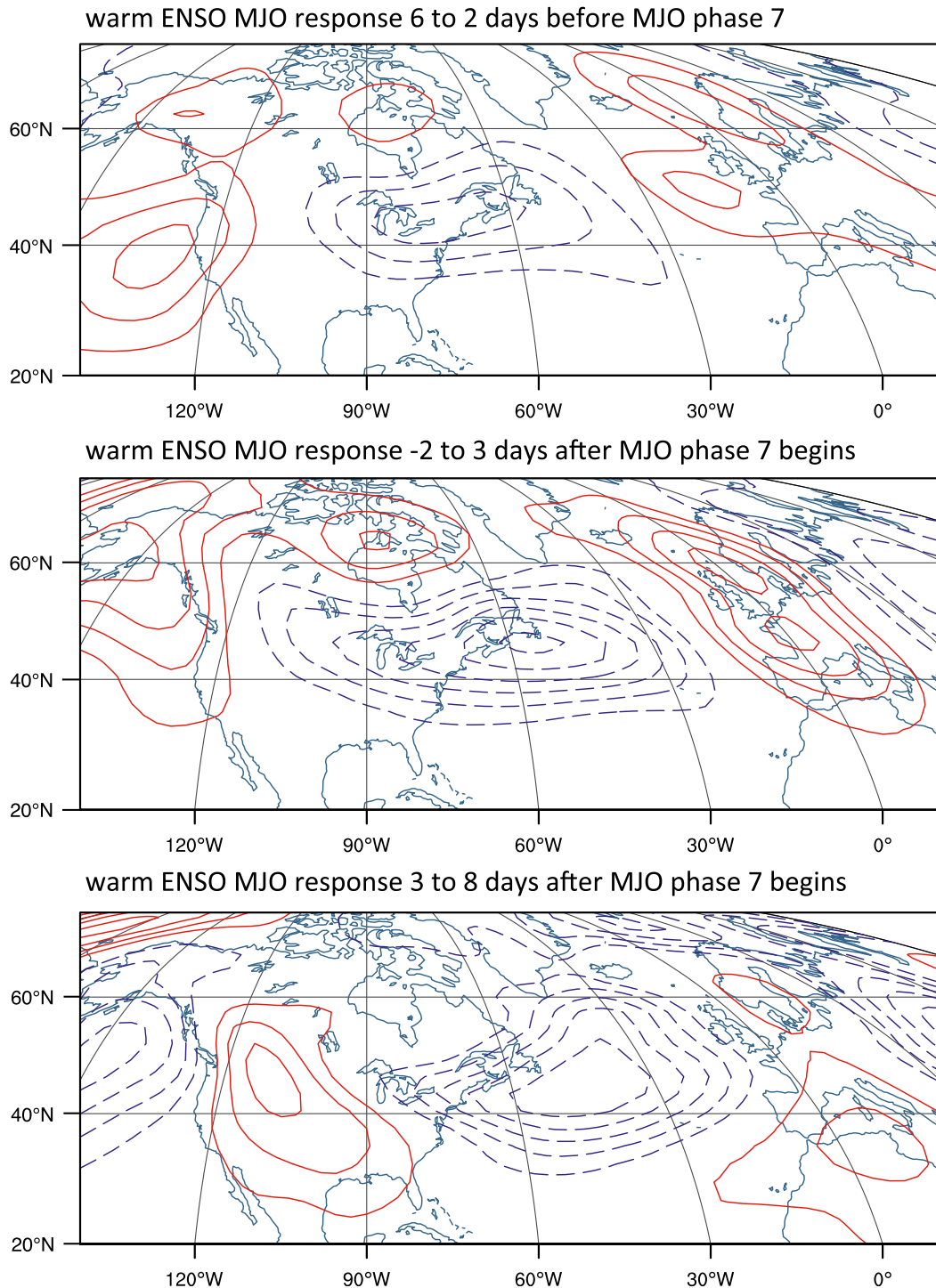


FIG. 17. NLBM 500-hPa geopotential height anomaly response against the warm ENSO basic state. Shown are the average (top) 16–20-, (middle) 20–25-, and (bottom) 25–30-day responses to a propagating heat source initiated with RMM phase 4. The averages approximately coincide with the days (top) prior to, (middle) during, and (bottom) after RMM phase 7, where phase 7 of the propagating heat source begins on day 22. See text for further details regarding the propagating heat source used. Contours are every 5 m and the zero contour is omitted.

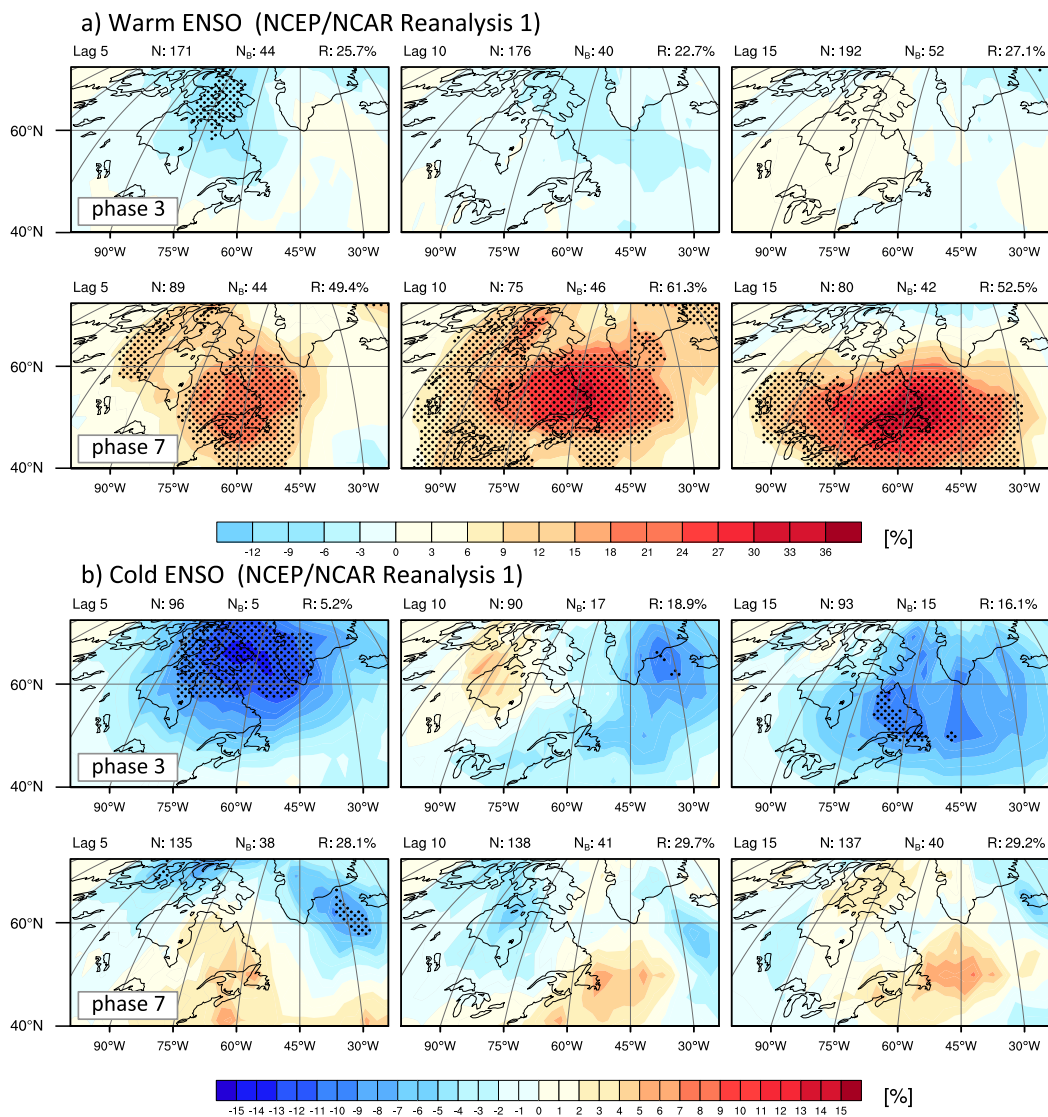


FIG. A1. Atlantic blocking frequency anomalies relative to the DJF mean computed using NCEP–NCAR Reanalysis 1 data from 1949–2016. Shown are frequency anomalies during (a) warm and (b) cold ENSO conditions (left to right) 5, 10, and 15 days after RMM (top) phase 3 and (bottom) phase 7. Black dotting indicates anomalies found to be 95% significantly different from zero. For explanation of the values above each panel, see section 5.

lower frequency of blocking in the mean relative to the high latitudes (e.g., H16) and are not discussed here due to sample size limitations. However, these regions could be examined using a GCM.

**Acknowledgments.** We are grateful to Paul Roundy and two anonymous reviewers for the insight and suggestions that lead to improvements in this manuscript, as well as to Masahiro Watanabe for providing the NLBM used in this study and Tetsu Nakamura for useful discussions on the NLBM. We also thank Masato Mori for LBM code modifications for the propagating heat source. This work was supported by the National Science Foundation under Grant AGS-1441916, and the NOAA

MAPP program under Grants NA16OAR4310064 and NA15OAR4310099. SAH was also funded in part by NSF Grant AGS-1624831. The statements, findings, conclusions, and recommendations do not necessarily reflect the views of the NSF.

## APPENDIX

### Addressing Sample Sizes

We address the limitation of sample size in two ways. One is by the use of the NLBM in section 6. Experiments using the NLBM suggest that the MJO teleconnection patterns shown in Figs. 6–8 are forced by MJO heating in

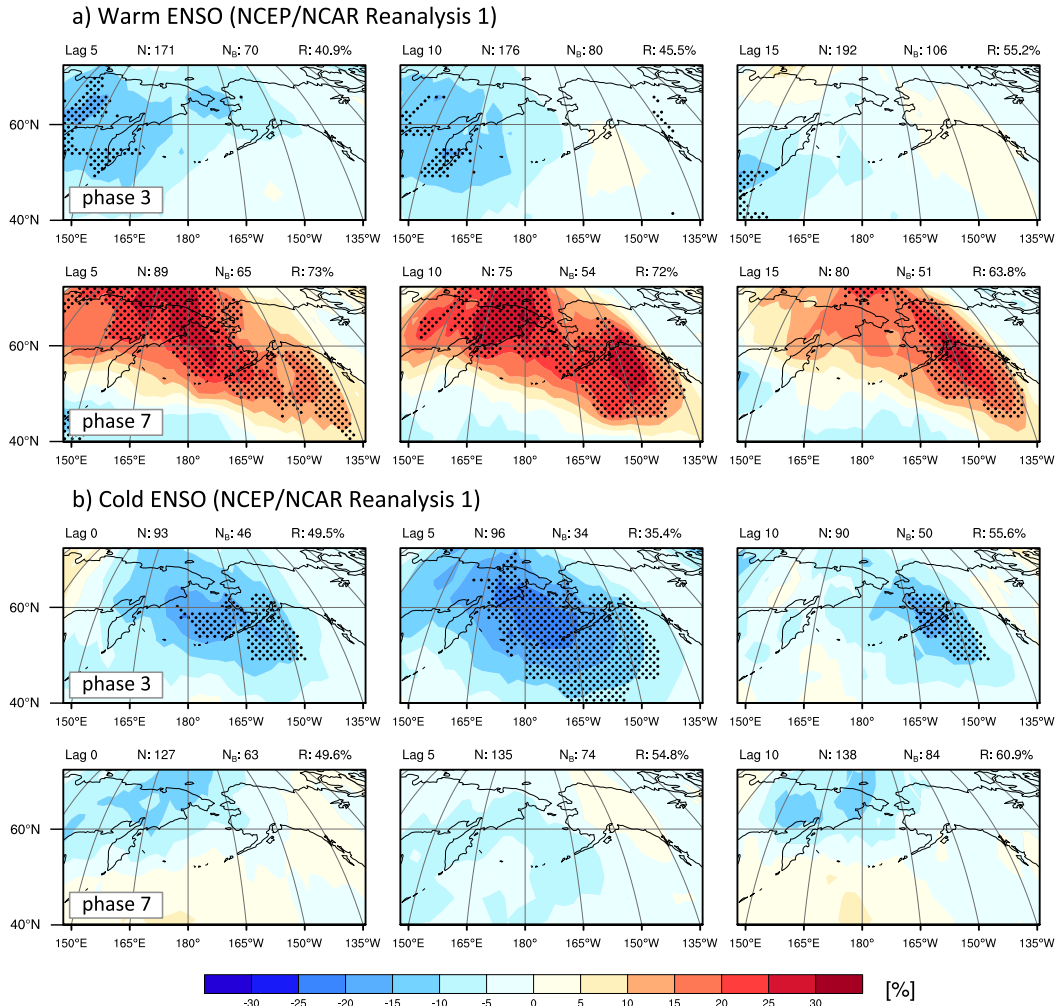


FIG. A2. As in Fig. A1, but for the Pacific basin.

an ENSO basic state. In this section, we address sample sizes a second way: by examining the anomalous blocking composites using a longer dataset. Here we recreate the results from section 5 using NCEP–NCAR Reanalysis 1 (NRR1) following the same methodology as described in section 2. The data have a  $2.5^\circ$  resolution and span from 1949 to 2016, with 16 warm ENSO events and 16 cold ENSO events defined in the same manner as the above analysis (see section 2a).

The NRR1 data span prior to the satellite era; therefore, in order to define the MJO RMM indices, only 200- and 850-hPa zonal winds are used and satellite-derived OLR is omitted. Using only the wind field is justified by the high correlation between the full RMM indices and the wind-only RMM indices ( $r = 0.99$ ; Straub 2013). To calculate the wind-based RMM indices, the equatorially averaged ( $15^\circ\text{S}$ – $15^\circ\text{N}$ ) NRR1 winds are projected onto the full combined EOFs, which include OLR. The EOFs

were made available by Matthew Wheeler (2015, personal communication). This methodology has been used in modeling studies to compare model MJOs to that of reanalysis, where the projection onto the provided reanalysis EOFs provides a consistent framework for comparison (e.g., Waliser et al. 2009; Henderson et al. 2017).

Atlantic blocking frequency anomalies during warm and cold ENSO events are shown in Figs. A1a and A1b, respectively, for RMM phases 3 and 7. Anomalies are defined as the difference from the NRR1 DJF mean blocking frequency (not shown). The results are very similar to Fig. 12. During warm ENSO events, there is a significant increase in Atlantic blocking frequency following RMM phase 7, although this increase extends farther south in the NRR1 dataset. Similar blocking anomaly composites were generated using the NRR1 data from 1979 to 2016 (not shown), and this southward

extent was still present, suggesting it is the NRR1 dataset and not the extended time-range that results in the southward extension. During cold ENSO events, Fig. A1b does not show a strong increase in phase 7 blocking frequency at later lags (e.g., Fig. 12b). However, the blocking frequency increase is amplified when limiting the NRR1 dataset to 1979–2016 (not shown), suggesting that the lag-15 increase (Fig. 12b) may be an artifact of a limited sample size. In agreement with Fig. 12, there is a stronger suppression of blocking following RMM phase 3 during cold ENSO events than during warm ENSO events. However, the region of significant suppression is not consistent between lags.

Similar composites were generated for the Pacific region (Fig. A2). The NRR1 composites demonstrate a persistent significant increase in blocking frequency following RMM phase 7 during warm ENSO events and not during cold ENSO events (Fig. A2a, bottom row), in agreement with Fig. 11. Similar to the Atlantic results, the persistent increase in NRR1 extends farther south in the east Pacific relative to ERA-Interim (Fig. 11a). Furthermore, the NRR1 composites show a persistent significant suppression of blocking following RMM phase 3 during cold ENSO events (Fig. A2b, top row). This significant suppression also extends farther south in the central and eastern Pacific. During warm ENSO events, the RMM phase 3 NRR1 composites demonstrate a significant decrease in blocking frequency over the northwest Pacific and northeastern Asia during lags 5 and 10 (Fig. A2a, top row). This significant suppression is not evident in the ERA-Interim composites (Fig. 11a) and is also not significant in the NRR1 1979–2016 blocking frequency composites (not shown).

Although these findings, in addition to the NLBM results, add confidence to our results, some caution is advised. The disagreements between the ERA-Interim and the NRR1 composites are largely in the magnitude of the blocking frequency, which at times are amplified (e.g., Fig. A2a, phase 3 lags 5–10) or weakened (e.g., Fig. A1b, phase 7, lag 15) in the longer NRR1 dataset relative to ERA-Interim. In general, however, the 1949–2016 NRR1 composites agree with the main findings presented in section 5.

#### REFERENCES

- Alaka, G. J., and E. D. Maloney, 2012: The influence of the MJO on upstream precursors to African easterly waves. *J. Climate*, **25**, 3219–3236, <https://doi.org/10.1175/JCLI-D-11-00232.1>.
- Barriopedro, D., R. García-Herrera, and R. M. Trigo, 2010: Application of blocking diagnosis methods to general circulation models. Part I: A novel detection scheme. *Climate Dyn.*, **35**, 1373–1391, <https://doi.org/10.1007/s00382-010-0767-5>.
- Berggren, R., B. Bolin, and C.-G. Rossby, 1949: An aerological study of zonal motion, its perturbations and break-down. *Tellus*, **1** (2), 14–37, <https://doi.org/10.1111/j.2153-3490.1949.tb01257.x>.
- Berrisford, P., B. J. Hoskins, and E. Tyrlis, 2007: Blocking and Rossby wave breaking on the dynamical tropopause in the Southern Hemisphere. *J. Atmos. Sci.*, **64**, 2881–2898, <https://doi.org/10.1175/JAS3984.1>.
- Buehler, T., C. C. Raible, and T. F. Stocker, 2011: The relationship of winter season North Atlantic blocking frequencies to extreme cold or dry spells in the ERA-40. *Tellus*, **63A**, 212–222, <https://doi.org/10.1111/j.1600-0870.2010.00492.x>.
- Capotondi, A., and Coauthors, 2015: Understanding ENSO diversity. *Bull. Amer. Meteor. Soc.*, **96**, 921–938, <https://doi.org/10.1175/BAMS-D-13-00117.1>.
- Cassou, C., 2008: Intraseasonal interaction between the Madden-Julian oscillation and the North Atlantic Oscillation. *Nature*, **455**, 523–527, <https://doi.org/10.1038/nature07286>.
- Davini, P., C. Cagnazzo, S. Gualdi, and A. Navarra, 2012: Bi-dimensional diagnostics, variability, and trends of Northern Hemisphere blocking. *J. Climate*, **25**, 6496–6509, <https://doi.org/10.1175/JCLI-D-12-00032.1>.
- Dee, D. P., and Coauthors, 2011: The ERA-Interim reanalysis: Configuration and performance of the data assimilation system. *Quart. J. Roy. Meteor. Soc.*, **137**, 553–597, <https://doi.org/10.1002/qj.828>.
- Green, J. S. A., 1977: The weather during July 1976: Some dynamical considerations of the drought. *Weather*, **32**, 120–126, <https://doi.org/10.1002/j.1477-8696.1977.tb04532.x>.
- Hamill, T. M., and G. N. Kiladis, 2014: Skill of the MJO and Northern Hemisphere blocking in GEFS and medium-range reforecasts. *Mon. Wea. Rev.*, **142**, 868–885, <https://doi.org/10.1175/MWR-D-13-00199.1>.
- Henderson, S. A., E. D. Maloney, and E. A. Barnes, 2016: The influence of the Madden-Julian oscillation on Northern Hemisphere winter blocking. *J. Climate*, **29**, 4597–4616, <https://doi.org/10.1175/JCLI-D-15-0502.1>.
- , —, and S.-W. Son, 2017: Madden-Julian oscillation Pacific teleconnections: The impact of the basic state and MJO representation in general circulation models. *J. Climate*, **30**, 4567–4587, <https://doi.org/10.1175/JCLI-D-16-0789.1>.
- Hendon, H. H., C. Zhang, and J. D. Glick, 1999: Interannual variation of the Madden-Julian oscillation during austral summer. *J. Climate*, **12**, 2538–2550, [https://doi.org/10.1175/1520-0442\(1999\)012<2538:IVOTMJ>2.0.CO;2](https://doi.org/10.1175/1520-0442(1999)012<2538:IVOTMJ>2.0.CO;2).
- Hoell, A., M. Barlow, M. C. Wheeler, and C. Funk, 2014: Disruptions of El Niño–Southern Oscillation teleconnections by the Madden-Julian oscillation. *Geophys. Res. Lett.*, **41**, 998–1004, <https://doi.org/10.1002/2013GL058648>.
- Hoskins, B. J., and D. J. Karoly, 1981: The steady linear response of a spherical atmosphere to thermal and orographic forcing. *J. Atmos. Sci.*, **38**, 1179–1196, [https://doi.org/10.1175/1520-0469\(1981\)038<1179:TSLROA>2.0.CO;2](https://doi.org/10.1175/1520-0469(1981)038<1179:TSLROA>2.0.CO;2).
- , and P. D. Sardeshmukh, 1987: A diagnostic study of the dynamics of the Northern Hemisphere winter of 1985–86. *Quart. J. Roy. Meteor. Soc.*, **113**, 759–778, <https://doi.org/10.1002/qj.49711347705>.
- , and T. Ambrizzi, 1993: Rossby wave propagation on a realistic longitudinally varying flow. *J. Atmos. Sci.*, **50**, 1661–1671, [https://doi.org/10.1175/1520-0469\(1993\)050<1661:RWPOAR>2.0.CO;2](https://doi.org/10.1175/1520-0469(1993)050<1661:RWPOAR>2.0.CO;2).
- Karoly, D. J., 1983: Rossby wave propagation in a barotropic atmosphere. *Dyn. Atmos. Oceans*, **7**, 111–125, [https://doi.org/10.1016/0377-0265\(83\)90013-1](https://doi.org/10.1016/0377-0265(83)90013-1).

- Kessler, W. S., 2001: EOF representations of the Madden–Julian oscillation and its connection with ENSO. *J. Climate*, **14**, 3055–3061, [https://doi.org/10.1175/1520-0442\(2001\)014<3055:EROTMJ>2.0.CO;2](https://doi.org/10.1175/1520-0442(2001)014<3055:EROTMJ>2.0.CO;2).
- Kosaka, Y., J. S. Chowdary, S.-P. Xie, Y.-M. Min, and J.-Y. Lee, 2012: Limitations of seasonal predictability for summer climate over East Asia and the northwestern Pacific. *J. Climate*, **25**, 7574–7589, <https://doi.org/10.1175/JCLI-D-12-00009.1>.
- Lee, H.-T., 2011: NOAA climate data record (CDR) of daily outgoing longwave radiation (OLR), 1979–2014, version 1.2. NOAA National Climatic Data Center, accessed 20 October 2015, <https://doi.org/10.7289/V5SJ1HH2>.
- Lin, H., G. Brunet, and J. Derome, 2009: An observed connection between the North Atlantic Oscillation and the Madden–Julian oscillation. *J. Climate*, **22**, 364–380, <https://doi.org/10.1175/2008JCLI2515.1>.
- , —, and R. Mo, 2010: Impact of the Madden–Julian oscillation on wintertime precipitation in Canada. *Mon. Wea. Rev.*, **138**, 3822–3839, <https://doi.org/10.1175/2010MWR3363.1>.
- Madden, R. A., and P. R. Julian, 1971: Detection of a 40–50 day oscillation in the zonal wind in the tropical Pacific. *J. Atmos. Sci.*, **28**, 702–708, [https://doi.org/10.1175/1520-0469\(1971\)028<0702:DOADOI>2.0.CO;2](https://doi.org/10.1175/1520-0469(1971)028<0702:DOADOI>2.0.CO;2).
- , and —, 1972: Description of global-scale circulation cells in the tropics with a 40–50 day period. *J. Atmos. Sci.*, **29**, 1109–1123, [https://doi.org/10.1175/1520-0469\(1972\)029<1109:DOGSCC>2.0.CO;2](https://doi.org/10.1175/1520-0469(1972)029<1109:DOGSCC>2.0.CO;2).
- Masato, G., B. J. Hoskins, and T. J. Woollings, 2012: Wave-breaking characteristics of midlatitude blocking. *Quart. J. Roy. Meteor. Soc.*, **138**, 1285–1296, <https://doi.org/10.1002/qj.990>.
- , —, and —, 2013: Winter and summer Northern Hemisphere blocking in CMIP5 models. *J. Climate*, **26**, 7044–7059, <https://doi.org/10.1175/JCLI-D-12-00466.1>.
- Matthews, A. J., B. J. Hoskins, and M. Masutani, 2004: The global response to tropical heating in the Madden–Julian oscillation during the northern winter. *Quart. J. Roy. Meteor. Soc.*, **130**, 1991–2011, <https://doi.org/10.1256/qj.02.123>.
- Moon, J.-Y., B. Wang, and K.-J. Ha, 2011: ENSO regulation of MJO teleconnection. *Climate Dyn.*, **37**, 1133–1149, <https://doi.org/10.1007/s00382-010-0902-3>.
- Moore, R. W., O. Martius, and T. Spengler, 2010: The modulation of the subtropical and extratropical atmosphere in the Pacific basin in response to the Madden–Julian oscillation. *Mon. Wea. Rev.*, **138**, 2761–2779, <https://doi.org/10.1175/2010MWR3194.1>.
- Nakamura, T., M. Hara, M. Oshika, and Y. Tachibana, 2015: Impact of the winter North Atlantic Oscillation (NAO) on the western Pacific (WP) pattern in the following winter through Arctic sea ice and ENSO. Part II: Multi-model evaluation of the NAO–ENSO linkage. *Climate Dyn.*, **45**, 3547–3562, <https://doi.org/10.1007/s00382-015-2556-7>.
- Pelly, J. L., and B. J. Hoskins, 2003: A new perspective on blocking. *J. Atmos. Sci.*, **60**, 743–755, [https://doi.org/10.1175/1520-0469\(2003\)060<0743:ANPOB>2.0.CO;2](https://doi.org/10.1175/1520-0469(2003)060<0743:ANPOB>2.0.CO;2).
- Pohl, B., and A. J. Matthews, 2007: Observed changes in the lifetime and amplitude of the Madden–Julian oscillation associated with interannual ENSO sea surface temperature anomalies. *J. Climate*, **20**, 2659–2674, <https://doi.org/10.1175/JCLI4230.1>.
- Rashid, H. A., H. H. Hendon, M. C. Wheeler, and O. Alves, 2011: Prediction of the Madden–Julian oscillation with the POAMA dynamical prediction system. *Climate Dyn.*, **36**, 649–661, <https://doi.org/10.1007/s00382-010-0754-x>.
- Rasmusson, E. M., and J. M. Wallace, 1983: Meteorological aspects of the El Niño/Southern Oscillation. *Science*, **222**, 1195–1202, <https://doi.org/10.1126/science.222.4629.1195>.
- Riddle, E. E., M. B. Stoner, N. C. Johnson, M. L. L’Heureux, D. C. Collins, and S. B. Feldstein, 2013: The impact of the MJO on clusters of wintertime circulation anomalies over the North American region. *Climate Dyn.*, **40**, 1749–1766, <https://doi.org/10.1007/s00382-012-1493-y>.
- Roundy, P. E., K. MacRitchie, J. Asuma, and T. Melino, 2010: Modulation of the global atmospheric circulation by combined activity in the Madden–Julian oscillation and the El Niño–Southern Oscillation during boreal winter. *J. Climate*, **23**, 4045–4059, <https://doi.org/10.1175/2010JCLI3446.1>.
- , N. Sakaeda, K. MacRitchie, and L. Gloeckler, 2017: Weather–climate interactions and MJO influences. *Climate Extremes: Patterns and Mechanisms*, Geophys. Monogr., Vol. 226, Amer. Geophys. Union, 139–163.
- Sakaeda, N., and P. E. Roundy, 2014: The role of interactions between multiscale circulations on the observed zonally averaged zonal wind variability associated with the Madden–Julian oscillation. *J. Atmos. Sci.*, **71**, 3816–3836, <https://doi.org/10.1175/JAS-D-13-0304.1>.
- Sardeshmukh, P. D., and B. J. Hoskins, 1988: The generation of global rotational flow by steady idealized tropical divergence. *J. Atmos. Sci.*, **45**, 1228–1251, [https://doi.org/10.1175/1520-0469\(1988\)045<1228:TGOGRF>2.0.CO;2](https://doi.org/10.1175/1520-0469(1988)045<1228:TGOGRF>2.0.CO;2).
- Seo, K.-H., and S.-W. Son, 2012: The global atmospheric circulation response to tropical diabatic heating associated with the Madden–Julian oscillation during northern winter. *J. Atmos. Sci.*, **69**, 79–96, <https://doi.org/10.1175/2011JAS3686.1>.
- , H.-J. Lee, and D. M. W. Frierson, 2016: Unraveling the teleconnection mechanisms that induce wintertime temperature anomalies over the Northern Hemisphere continents in response to the MJO. *J. Atmos. Sci.*, **73**, 3557–3571, <https://doi.org/10.1175/JAS-D-16-0036.1>.
- Small, D., E. Atallah, and J. R. Gyakum, 2014: An objectively determined blocking index and its Northern Hemisphere climatology. *J. Climate*, **27**, 2948–2970, <https://doi.org/10.1175/JCLI-D-13-00374.1>.
- Straub, K. H., 2013: MJO initiation in the real-time multivariate MJO index. *J. Climate*, **26**, 1130–1151, <https://doi.org/10.1175/JCLI-D-12-00074.1>.
- Takahashi, C., and R. Shirooka, 2014: Storm track activity over the North Pacific associated with the Madden–Julian oscillation under ENSO conditions during boreal winter. *J. Geophys. Res. Atmos.*, **119**, 6663–6683, <https://doi.org/10.1002/2014JD021973>.
- Takaya, K., and H. Nakamura, 2001: A formulation of a phase-independent wave-activity flux for stationary and migratory quasigeostrophic eddies on a zonally varying basic flow. *J. Atmos. Sci.*, **58**, 608–627, [https://doi.org/10.1175/1520-0469\(2001\)058<0608:AFOAPI>2.0.CO;2](https://doi.org/10.1175/1520-0469(2001)058<0608:AFOAPI>2.0.CO;2).
- Tibaldi, S., and F. Molteni, 1990: On the operational predictability of blocking. *Tellus*, **42A**, 343–365, <https://doi.org/10.3402/tellusa.v42i3.11882>.
- Trenberth, K. E., 1986: An assessment of the impact of transient eddies on the zonal mean flow during a blocking episode using localized Eliassen–Palm flux diagnostics. *J. Atmos. Sci.*, **43**, 2070–2087, [https://doi.org/10.1175/1520-0469\(1986\)043<2070:AAOTIO>2.0.CO;2](https://doi.org/10.1175/1520-0469(1986)043<2070:AAOTIO>2.0.CO;2).

- Tseng, K.-C., E. A. Barnes, and E. D. Maloney, 2018: Prediction of the midlatitude response to strong Madden–Julian oscillation events on S2S time scales. *Geophys. Res. Lett.*, **45**, 763–470, <https://doi.org/10.1002/2017GL075734>.
- Waliser, D., and Coauthors, 2009: MJO simulation diagnostics. *J. Climate*, **22**, 3006–3030, <https://doi.org/10.1175/2008JCLI2731.1>.
- Watanabe, M., and M. Kimoto, 2000: Atmosphere–ocean thermal coupling in the North Atlantic: A positive feedback. *Quart. J. Roy. Meteor. Soc.*, **126**, 3343–3369, <https://doi.org/10.1002/qj.49712657017>.
- Wheeler, M. C., and H. H. Hendon, 2004: An all-season real-time multivariate MJO index: Development of an index for monitoring and prediction. *Mon. Wea. Rev.*, **132**, 1917–1932, [https://doi.org/10.1175/1520-0493\(2004\)132<1917:AARMMI>2.0.CO;2](https://doi.org/10.1175/1520-0493(2004)132<1917:AARMMI>2.0.CO;2).
- Wilks, D. S., 2011: *Statistical Methods in the Atmospheric Sciences*. 3rd ed. Elsevier, 676 pp.
- Woollings, T., and B. Hoskins, 2008: Simultaneous Atlantic–Pacific blocking and the northern annular mode. *Quart. J. Roy. Meteor. Soc.*, **134**, 1635–1646, <https://doi.org/10.1002/qj.310>.
- , —, M. Blackburn, and P. Berrisford, 2008: A new Rossby wave-breaking interpretation of the North Atlantic Oscillation. *J. Atmos. Sci.*, **65**, 609–626, <https://doi.org/10.1175/2007JAS2347.1>.
- Yanai, M., S. Esbensen, and J.-H. Chu, 1973: Determination of bulk properties of tropical cloud clusters from large-scale heat and moisture budgets. *J. Atmos. Sci.*, **30**, 611–627, [https://doi.org/10.1175/1520-0469\(1973\)030<0611:DOBPOT>2.0.CO;2](https://doi.org/10.1175/1520-0469(1973)030<0611:DOBPOT>2.0.CO;2).
- Yasui, S., and M. Watanabe, 2010: Forcing processes of the summertime circumglobal teleconnection pattern in a dry AGCM. *J. Climate*, **23**, 2093–2114, <https://doi.org/10.1175/2009JCLI3323.1>.